High-resolution cryo-EM structure of urease from the pathogen *Yersinia enterocolitica*

Ricardo D. Righetto[1*], Leonie Anton[2*], Ricardo Adaixo[1*], Roman P. Jakob[2], Jasenko Zivanov[1], Mohamed-Ali Mahi[2,3], Philippe Ringler[1], Torsten Schwede[2,3], Timm Maier[2†] and Henning Stahlberg[1†]

[1] Center for Cellular Imaging and NanoAnalytics, Biozentrum, University of Basel, Mattenstrasse 26, CH-4058 Basel, Switzerland.

[2] Biozentrum, University of Basel, Klingelbergstrasse 50/70, CH-4056 Basel, Switzerland.

[3] SIB Swiss Institute of Bioinformatics, Biozentrum, University of Basel, Klingelbergstrasse 50/70, CH-4056 Basel, Switzerland.

[*] *these authors contributed equally to this work.*

[†] Corresponding authors:

Timm Maier
Biozentrum, University of Basel
Klingelbergstrasse 50/70
CH-4056 Basel, Switzerland
Phone: +41 61 207 21 76
E-mail: timm.maier@unibas.ch

Henning Stahlberg
Center for Cellular Imaging and NanoAnalytics (C-CINA)
Biozentrum, University of Basel
WRO-1058, Mattenstrasse 26
CH-4058 Basel, Switzerland
Phone: +41 61 387 32 62
E-mail: henning.stahlberg@unibas.ch

Running title: Cryo-EM structure of *Y. enterocolitica* urease

Keywords: urease; enzyme; metalloprotein; radiation damage; cryo-electron microscopy;

Abstract

Urease converts urea into ammonia and carbon dioxide and makes urea available as a nitrogen source for all forms of life except animals. In human bacterial pathogens, ureases also aid in the invasion of acidic environments such as the stomach by raising the surrounding pH. Here, we report the structure of urease from the pathogen *Yersinia enterocolitica* at better than 2 Å resolution from cryo-electron microscopy. *Y. enterocolitica* urease is a dodecameric assembly of a trimer of three protein chains, ureA, ureB and ureC. The high data quality enables detailed visualization of the urease bimetal active site and of the impact of radiation damage. Our data are of sufficient quality to support drug development efforts.

42 ## Introduction

43 Ureases are nickel-metalloenzymes produced in plants, fungi and bacteria, but not in
44 animals. They facilitate nitrogen fixation by metabolizing urea, but in some pathogenic
45 bacteria they serve a dual function and consume ammonia to promote survival in acidic
46 environments. This function is vital during host infection where the bacteria have to survive
47 the low pH of the stomach (Gripenberg-Lerche *et al.*, 2000), and of phagosomes in host
48 cells (Young *et al.*, 1996; Maroney & Ciurli, 2014). The relevance of ureases in early stages
49 of infection renders them attractive targets for novel anti-microbials.

50 Ureases catalyze the breakdown of urea into ammonia and carbamate at a rate 10^{14} to 10^{15}
51 times faster than the non-catalyzed reaction **(Fig. 1a)**, and are arguably the most efficient
52 hydrolases (Maroney & Ciurli, 2014). In a second non-catalyzed step, carbamate is
53 spontaneously hydrolyzed to yield another molecule of ammonia as well as one molecule of
54 bicarbonate (Mazzei *et al.*, 2017). Jack bean urease was the first enzyme to be crystallized,
55 offering evidence that enzymes are proteins (Sumner, 1926) and was the first
56 metalloenzyme to be shown to use nickel in its active site (Dixon *et al.*, 1975). All ureases
57 characterized to date share the architecture of their active site (Kappaun *et al.*, 2018). Two
58 Ni^{2+} ions in the active site are coordinated by a carbamylated lysine, four histidines and one
59 aspartate. Urea first interacts with Ni(1) through its carbonyl oxygen, making urea more
60 available for nucleophilic attacks. The amino nitrogen then binds to Ni(2) and a proton is
61 transferred from a water molecule to the amine in a nucleophilic attack on the carbonyl
62 carbon of urea. The active site is closed off during the reaction by a conformationally variable
63 helix-turn-helix motif, referred to as the mobile flap. Despite their common catalytic
64 mechanism, ureases display different chain topologies and higher order oligomeric
65 assemblies **(Fig. 1b,c)**. Jack bean urease assembles into an oligomer of a single type of
66 polypeptide chain with D3 symmetry ($[[\alpha]_3]_2$ D3) **(Fig. 1b,c)** (Maroney & Ciurli, 2014). The

urease of the human pathogen *Helicobacter pylori* is composed of two types of polypeptide chains (ureA, ureB) and assembles into a dodecamer (tetramer-of-trimers) with tetrahedral symmetry ($[[\alpha\beta]_3]_4$ T) **(Fig. 1b,c)**. The ability of ureases to raise the pH of their environment benefits *H. pylori* in colonizing the stomach and downstream gut, causing gastric ulcers (Kappaun *et al.*, 2018). The urease of the opportunistic pathogen *Klebsiella aerogenes* (Podschun & Ullmann, 1998) assembles into a heterotrimer of three proteins ureA, ureB and ureC, which in turn oligomerizes into a trimer ($[\alpha\beta\gamma]_3$ C3) (Jabri *et al.*, 1995) **(Fig 1b,c)**. This oligomeric assembly is common also to most other structurally characterized bacterial ureases (Maroney & Ciurli, 2014).

Yersinia enterocolitica is the causative agent of yersiniosis, a gastrointestinal infection, reactive arthritis and erythema nodosum. The infection spreads to humans through consumption of contaminated food with pigs being one of the largest reservoirs of *Y. enterocolitica*. The symptoms of yersiniosis are fever, abdominal pain, diarrhea and/or vomiting and is one of the most reported enteritis in some countries, although outbreaks are rare (Drummond *et al.*, 2012). *Y. enterocolitica* is a facultative intracellular bacterium and can survive in very different environments. In the presence of urea *Y. enterocolitica* can tolerate extremely acidic conditions (Young *et al.*, 1996). *Y. enterocolitica* urease comprises three polypeptide chains (ureA, ureB and ureC), an architecture similar to that of *K. aerogenes* urease **(Fig. 1b)**.

Here we present the structure of *Y. enterocolitica* urease at an overall resolution of 1.98 Å, which was achieved using recent advances in cryo-EM data collection and processing. The structure shows that *Y. enterocolitica* urease assembles into a dodecameric hollow sphere with $[[\alpha\beta\gamma]_3]_4$ T oligomeric assembly structure **(Fig. 2)**. A tightly embedded kinked loop is interacting with neighboring domains and is potentially responsible for the assembly of the oligomer. The data allows model building of the active site carbamylated lysine, visualization of radiation damage to the nickel-metal center, and hydration networks throughout the

93 protein. Our work highlights the potential of cryo-EM for structure-based drug discovery,
94 specifically for large enzyme assemblies, which have been historically difficult to analyze by
95 X-ray crystallography.

96

97 Results & Discussion

98 Structure determination of *Y. enterocolitica* urease by cryo-EM

99 We have used single particle cryo-EM to determine the structure of the fully assembled *Y.*
100 *enterocolitica* urease. We acquired 4,494 movies of urease particles using a Titan Krios
101 transmission electron microscope (TEM) equipped with a K2 direct electron detector and an
102 energy filter (see **Methods** for details). Approximately half of the movies (2,243) were
103 acquired by illuminating three locations ("shots") per grid hole using beam-image shift in
104 order to speed up the data collection (Cheng *et al.*, 2018), whereas the remaining movies
105 were recorded without this feature i.e. just a single shot at the center of the hole. This allowed
106 us to measure and assess the extent of beam tilt and other optical aberrations, as well as
107 the behavior of sample drift between each condition and beam-image shift position. Typical
108 micrographs from the imaged grids are shown in **Supp. Fig. 1a** and a summary of data
109 collection information is given in **Supp. Tab. 1**.
110 Each dataset was processed separately for 3D reconstruction following the strategy
111 depicted in **Supp. Fig. 2**. The first obtained 3D map, at an overall resolution of 2.6 Å,
112 revealed that this urease assembly is a dodecamer of tetrahedral (T) symmetry with a
113 diameter of approximately 170 Å. The separate processing of each dataset yielded refined
114 3D maps at nominal resolutions of 2.10 Å and 2.20 Å for the multi-shot and single-shot
115 cases, respectively (see **Methods**).
116 For comparison, we also processed the merged set of particles from both datasets
117 altogether. We observed on the 2D class averages a preferential orientation for the three-
118 fold symmetric view of urease, and also the presence of isolated monomers and broken

119 assemblies **(Supp. Fig. 1b)**. The presence of such incomplete assemblies was further
120 confirmed by performing 3D classification without imposing symmetry, as shown in
121 **Supp. Fig. 1c**. The 3D class corresponding to the complete dodecameric assembly of
122 urease contained 119,020 particles, of which 69,512 (58.4%) came from the multi-shot and
123 49,518 (41.6%) from the single-shot dataset. With respect to the number of particles picked
124 from each dataset, 64.7% of the particles from the multi-shot and 56.8% from the single-
125 shot datasets were retained at this stage and throughout the final reconstruction. While
126 coma-free alignment was performed and active beam-tilt compensation in SerialEM (Schorb
127 *et al.*, 2019) was used on our data collections, after performing beam tilt refinement in
128 RELION-3 (Zivanov *et al.*, 2018) we observed that the single-shot case has a residual beam-
129 tilt higher than the smallest residual observed in the multi-shot case **(Supp. Tab. 2)**. These
130 two values are however very close to zero and are possibly within the error margin of the
131 *post hoc* beam tilt refinement procedure.
132 The reduced need to move the specimen stage in beam-image shift mode not only speeds
133 up data collection but also minimizes stage drift. The second and third shots from the multi-
134 shot dataset have comparatively less drift than both the first multi-shot and the single shot,
135 as suggested by the parameter values obtained from the Bayesian polishing training
136 (Zivanov *et al.*, 2019*a*) on each beam-tilt class separately **(Supp. Tab. 3)**. As all the three
137 multi-shots are taken in nearby areas within the same foil hole, this observation is consistent
138 with the annealing of the vitreous ice layer and its carbon support after pre-irradiating the
139 specimen as reported previously (Brilot *et al.*, 2012).
140 At this point, the nominal resolution of the map after 3D refinement was 2.05 Å. Finally,
141 correcting for residual higher-order aberrations in CTF refinement (Zivanov *et al.*, 2019*b*)
142 **(Supp. Fig. 3)** yielded a map at a global resolution of 1.98 Å **(Supp. Fig. 4a)**. Local
143 resolution estimation reveals that the core of the map is indeed at this resolution level or
144 better **(Fig. 2a and Supp. Fig. 4b)**, and the local resolution-filtered map was then used for

145 model building as explained in the next section. Despite the twelve-fold symmetry of the
146 urease assembly, a limiting factor in the resolution of the map is the strong presence of
147 preferential orientation, as confirmed by the plot of the final orientation assignments
148 (**Supp. Fig. 4c**). The estimated angular distribution efficiency is 0.60 (Naydenova & Russo,
149 2017). An overview of the cryo-EM map and its main features are depicted in **Supp. Mov. 1.**
150

151 ***Y. enterocolitica* urease assembles as a tetramer of trimers**

152 Model building was initiated from available crystallographic models with subsequent fitting
153 and refinement against the cryo-EM map. The model was built and refined for one
154 asymmetric unit containing one copy of the ureA, ureB and ureC protein each. The model
155 was then expanded using NCS (see **Methods**). The complete model covering the whole
156 oligomeric assembly contains 9,552 residues, 3,672 waters and 24 nickel ions (two per
157 active site, twelve active sites) **(Table 1)**. The quality of the model was assessed with the
158 cryo-EM validation tools in the PHENIX package (Afonine, Klaholz *et al.*, 2018). The map
159 allowed for the building of all residues of ureA (1-100), and residues 31-162 of ureB and 2-
160 327/335-572 of ureC **(Supp. Fig. 5)**. The hetero-trimer formed by the three protein chains
161 (ureA, ureB, ureC) **(Fig. 1b)** oligomerizes into a homo-trimer. The homo-trimer is arranged
162 in a tetramer-of-trimers making the full complex a dodecamer of the hetero-trimer **(Fig. 2b)**.
163 There are four large oval shaped holes between the trimers (64 Å long, 12 Å wide, high
164 electrostatic potential) and four smaller holes at the center of the trimer with a diameter of 6
165 Å (low electrostatic potential), as shown in **Fig. 2b**, and the center of the enzyme assembly
166 is hollow **(Fig. 2).** The holes provide ample opportunity for diffusion of the uncharged
167 substrate and product, and the hollow inside potentially leads to local increase of reaction
168 product. The assembly has the same symmetry as the urease homologue in *H. pylori*, which
169 was postulated to increase stability and/or resistance to acidic environments
170 (Ha *et al.*, 2001).

171

172 For analysis of the protein sequences, the ConSurf Server (Berezin *et al.*, 2004; Ashkenazy
173 *et al.*, 2016) was used with the sample list of homologs option to get a diverse set of 150
174 sequences. The protein chains of *Y. enterocolitica* urease are highly conserved across
175 different organisms. The ureA chain is split after a LVTXXXP motif and is 99-100 amino
176 acids long in most cases, with a sequence identity of 55.7%. The ureB chain of *Y.*
177 *enterocolitica* has between 20 and 30 N-terminal amino acids more compared to the other
178 sequences (except *Kaistia sp.* SCN 65-12), which share an identity of 51.5%. This N-
179 terminal extension is located on the outside of the holoenzyme where ureA and ureB chain
180 split occurs and are too disordered to be modeled in the structure **(Supp. Fig. 5)**. The
181 charges and properties of this stretch of amino acids vary and if they still serve a function
182 remains unclear. The last 20 amino acids of the C-terminus of ureB are only represented in
183 half of the compared sequences and accurate sequence conservation could not be
184 determined in this part. This stretch contains a loop and a C-terminal helix **(Supp. Fig. 5)**.
185 The ureC protein of the compared sequences has a shared sequence identity of 60.3%. All
186 amino acids involved in catalysis are highly conserved **(Supp. Fig. 5)**. The ureA and ureB
187 chains show lower conservation compared to ureC. They are not involved in catalysis but in
188 scaffolding, so the differences could stem from their role in different types of oligomeric
189 assembly **(Fig. 3)**.
190 To investigate this aspect further, we compared the presented structure to the ureases of *H.*
191 *pylori*, *S. pasteurii* and *K. aerogenes*. Sequence identity scores among these ureases are
192 provided in **Supp. Tab. 4**. The *H. pylori* urease is made up of two protein chains ureA (that
193 contains the equivalent of ureA and ureB in *Y. enterocolitica*) and ureB (that is the equivalent
194 of ureC in *Y. enterocolitica*) **(Fig. 1c and Fig. 3c)**. It assembles into a T-symmetric oligomer
195 like in *Y. enterocolitica* and the crystal structure was solved to 3 Å. *S. pasteurii* and *K.*
196 *aerogenes* ureases both assemble into a trimer from the hetero-trimeric unit **(Fig. 1c and**

197 **Fig. 3b)**. *S. pasteurii* was solved in the presence of the inhibitor N-(n-Butyl)thiophosphoric
198 Triamid (NBPT) to 1.28 Å (Mazzei *et al.*, 2017). The crystal structure of *Klebsiella aerogenes*
199 was solved to 1.9 Å as in absence of substrate or inhibitors (Jabri *et al.*, 1995).
200 There are two main regions with high root mean square deviations (RMSDs) when
201 comparing these three ureases to the *Y. enterocolitica* model **(Supp. Fig. 6 and Supp. Tab.**
202 **5)**. The first region with high deviation is the mobile flap, which opens and closes over the
203 active site (residues 312 to 355 of ureC). The residues of its connecting loop could not be
204 built with confidence in the cryo-EM model (residues 326 to 333 of ureC). The other region
205 with large differences is on the edges of ureA and ureB where the interactions with the next
206 protomer occur. The *H. pylori* assembly contains an additional C-terminal loop (residues
207 224-238 of ureA) after the top alpha helix (residues 206-223 of ureA). This helix (central
208 helix) forms the three-fold axis of three neighboring trimers and the loop binds in a head-to-
209 tail fashion to the next trimer forming the tetramer **(Fig. 3a,c)** (Ha *et al.*, 2001). The core of
210 the assembly is identical in its structure. For whole-chain superposition scores and RMSD
211 values between the compared models please see **Supp. Tab. 5**.
212 In the dodecameric assembly seven different interfaces are formed between the hetero-
213 trimers **(Fig. 4a,b and Supp. Fig. 7)**. Intra-trimer interactions occur between the three basic
214 hetero-trimers in one assembled trimer, forming a three-fold symmetry axis **(Fig. 4a)**. The
215 interactions between these trimers to form the tetramer then make up a different three-fold
216 symmetry axis **(Fig. 4b)**. The three largest interfaces (interfaces 1-3) are formed intra-
217 trimeric between ureC of one hetero-trimer and ureC, ureA and ureB of the next trimer **(Fig.**
218 **4a)**. The three ureA proteins make up the intra-trimer-core (first three-fold axis) with interface
219 4 **(Fig. 4c and Supp. Fig. 7)**. Comparison of the interface areas formed in the trimer
220 assembly shows no substantial differences between the four organisms **(Supp. Fig. 7)**.
221 Inter-trimer interfaces (interfaces 5, 6, 7) formed in the dodecameric *Y. enterocolitica* and *H.*
222 *pylori* ureases have similar areas **(Fig. 4b and Supp. Fig. 7)**. Part of the interactions occur

223 between ureB and ureC forming interfaces with each other (interface 4, 6). The other
224 interaction is between the three ureB proteins and forms interface 7 and the inter-trimer-
225 core (second three-fold axis) with their central helices **(Fig. 4b)**. *Y. enterocolitica* does not
226 have the same oligomerization loop after the central helix proposed for *H. pylori*. However,
227 there is a short loop before the central helix, which is extended in *Y. enterocolitica*. It binds
228 into a pocket of ureC of the neighboring trimer in interface 6 **(Fig. 4e)**. These types of loops
229 or extensions are missing from *S. pasteurii* and *K. aerogenes* ureB proteins. *S. pasteurii* has
230 the central helix, but there is no extended loop before or after it **(Supp. Fig. 6b)**. *K.*
231 *aerogenes* urease does not have a helix nor a loop in this region **(Fig. 3b)**. This suggests
232 that the presence of oligomerization loops in ureB is crucial for determining the oligomeric
233 state of the enzyme.
234 The dodecameric holoenzyme structure of ureases might aid in stabilizing the protein at
235 acidic pH, and in combination with 12 active sites producing ammonia enables the formation
236 of a pH-neutralizing microenvironment around the assembly (Ha *et al.*, 2001). This ensures
237 the continued function of the enzyme and makes this type of oligomeric assembly essential
238 to survival of *Y. enterocolitica* in the host. It is remarkable that *Y. enterocolitica* is the first
239 organism outside the Helicobacteraceae family to have a known dodecameric urease.
240 Considering the different subunit organization between these ureases, it raises the question
241 of what particular events in the evolutionary history of *Y. enterocolitica* could have led to this
242 type of assembly (Ligabue-Braun *et al.*, 2013).
243

244 **The empty active site is filled with water**

245 At the global resolution of 1.98 Å, detailed structural features can be observed. All
246 throughout the highly resolved areas of the protein, salt bridges, backbone and side chain
247 hydration and alternative side chain conformations can be visualized **(Supp. Fig. 8a-c)**.
248 Furthermore, the high resolution allows for a detailed description of the nickel-metallo-center

249 and the active site. The active site is located on the ureC protein at the edge of the hetero-
250 trimer and is wedged in between the ureA and ureB proteins of the next hetero-trimer in the
251 homo-trimeric assembly **(Fig. 5a)**.
252 The catalysis of ammonia and carbamate from urea occurs in two steps **(Fig. 1a)**. Urea first
253 interacts with the nickel ions through its carbonyl oxygen and amino nitrogens. The active
254 site contains two Ni^{2+} ions which are coordinated by six different amino acids **(Fig. 5b)**. Both
255 Ni^{2+} ions are coordinated by the carbamylated LYS222*. Ni(1) is additionally coordinated by
256 HIS224, HIS251 and HIS277 and Ni(2) by HIS139, HIS141 and ASP365. Close to the active
257 site is a methionine (MET369), which can be modelled in different alternative conformations.
258 One conformation could potentially reach the active site. There is no described function for
259 this amino acid **(Fig. 5c and Supp. Fig. 9)**.
260 The active site is protected by a helix-turn-helix motif, called the mobile-flap. Its function is
261 to coordinate the access of substrate to the catalytic site and the release of the product from
262 it (Maroney & Ciurli, 2014). After closing of the mobile flap, a proton is transferred from a
263 water molecule to the other amine in a nucleophilic attack on the carbonyl carbon of urea.
264 A conserved histidine on the mobile flap (HIS325) is essential for catalysis by possibly acting
265 as a general acid and aiding in deprotonation **(Fig. 5a)** (Maroney & Ciurli, 2014; Kappaun *et*
266 *al.*, 2018). By closing of the mobile flap the HIS325 moves closer to the active site, also
267 stabilizing urea in the active site pocket (Maroney & Ciurli, 2014). Flap opening then releases
268 ammonia and carbamate, where the latter spontaneously hydrolyses into another molecule
269 of ammonia and bicarbonate. The mobile flap of the cryo-EM structure presented here is in
270 an open position, which is explained by the absence of substrate or inhibitors in the sample
271 **(Fig. 5a)**. Coordinated water molecules can be seen in the empty pocket of the active site,
272 which do not only form hydrogen bonds with side chains or the protein backbone, but also
273 with each other constituting a hydration network **(Supp. Fig. 8d)**.
274 The resolution in the active site is sufficient for complete atomic description of the

275 coordinated Ni^{2+} ions, including the carbamylated lysine. The protonation states of the active
276 site residues are also represented in the map **(Fig. 5b)**. One of the hydroxide molecules in
277 the active site is essential as it performs the nucleophilic attack on urea while other
278 molecules are displaced by urea and the closing of the mobile flap (Kappaun *et al.*, 2018).
279 Comparison to the crystal structure of *K. aerogenes* of similar nominal resolution (1.9 Å)
280 shows differences in the visualization of these features. This crystal structure was solved in
281 absence of inhibitors or substrate such that the active site is also empty and the mobile flap
282 in an open conformation **(Fig. 5a)**. The details of the map provides finer details around the
283 Ni^{2+} ions in the cryo-EM map than the crystallographic data. The protonation of the histidines
284 is clearly visible in the cryo-EM density **(Fig. 5b)**. The positions of the side chains and the
285 Ni^{2+} ions in the active site are very similar to the *Y. enterocolitica* urease structure with a
286 RMSD of 0.270 Å **(Supp. Tab. 5)**. The *S. pasteurii* crystal structure was solved in presence
287 of the inhibitor NBPT which displaces the essential water molecules needed for the reaction
288 from the active site. The closing of the mobile flap displaces the rest of the waters and brings
289 the catalytic HIS323 closer to the active site. The tight packing of side chains prevents urea
290 from entering the active site, efficiently blocking it **(Fig. 5b,e)**. The active site residues and
291 Ni^{2+} ions have a RMSD of 0.293 Å between *S. pasteurii* and *Y. enterocolitica*.
292

293 **Nickel atoms come closer together**

294 The distance between the Ni^{2+} ions is 3.7 Å in X-ray structures of *K. aerogenes* and *S.*
295 *pasteurii*, but only 3.2 Å in the *Y. enterocolitica* cryo-EM model **(Fig. 5b,d)**. Short distances
296 of 3.1-3.3 Å were described for *S. pasteurii* and *K. aerogenes* at high resolutions for
297 structures in presence of β-Mercaptoethanol (β-ME) (Benini *et al.*, 1998). Knowing that
298 metallic cores are particularly sensitive to radiation (Yano *et al.*, 2005), we tried to determine
299 the extent to which radiation damage can explain the shorter distance between the Ni^{2+} ions.
300 For this purpose, we generated per-frame reconstructions for the first 25 frames of our data

301 collection and refined the model on each of them (see **Methods**) and measured the
302 distances between the residues involved in ion coordination, shown in **Fig. 6**. At the
303 beginning of the exposure, in which the frames contribute more to the full reconstruction due
304 to dose-weighting (Grant & Grigorieff, 2015; Zivanov *et al.*, 2019*a*), there is a trend of the
305 ions coming closer together (**Fig. 6a-i**). While we cannot determine exactly how this arises
306 from radiation damage, it is likely a result of several interactions in the active site changing
307 simultaneously along the exposure. For example, both Ni(1) and Ni(2) tend to come closer
308 to the carbamylated LYS222 (**Fig. 6a-iv,v**) as ASP365 vanishes (**Fig. 6a-vi**), which can be
309 seen in the **Supp. Mov. 2**. Aspartic acid is known to have its side chain damaged very early
310 on (Hattne *et al.*, 2018). The dynamic interplay between residues along the exposure (**Fig.
311 6b**) is likely due to the different rates at which specific types of bonds and residues are
312 damaged (Fromm *et al.*, 2015): first negatively charged residues, then positively charged
313 ones followed by aromatic side chains, as also observed in **Supp. Mov. 2**. However, the
314 later part of the exposure must be interpreted with caution, as atomic coordinates become
315 less reliable, which is verified by the overall increase in B-factors in **Fig. 6c** and the error
316 bars in **Fig. 6a**.

317 Conclusion

318 Large urease assemblies have been historically difficult to study by X-ray crystallography
319 (Ha *et al.*, 2001). We have determined the structure of a dodecameric urease assembly, a
320 metalloenzyme from the pathogen *Y. enterocolitica* at an overall resolution of 1.98 Å using
321 cryo-EM. The collection of datasets with and without beam-image shift demonstrates the
322 advantages of using this feature of modern TEMs and invites further investigations on the
323 behavior of optical aberrations and specimen drift.

324 Our results demonstrate the feasibility of cryo-EM as a technique for obtaining structures of
325 clinically relevant enzymes with sufficient quality for *de novo* model building and drug design.

326 The cryo-EM map has allowed a detailed description of the active site and the oligomeric
327 assembly. More specifically, we could observe the putative oligomerization loop that enables
328 the dodecameric assembly, which was hypothesized to be responsible for the enhanced
329 survival of *Y. enterocolitica* in highly acidic environments (Young *et al.*, 1996). This urease
330 is the first outside the Helicobacteraceae family, and therefore without an αβ subunit
331 organization, to have a dodecameric assembly reported. What evolutionary events have led
332 to this intriguing combination of subunit organization and quaternary structure are unknown.

333 Furthermore, in comparison to the *K. aerogenes* structure, which is at approximately the
334 same nominal resolution, the cryo-EM map offers an improved representation of protons
335 and Ni^{2+} ions. A possible explanation is that the error in the phases derived in the X-ray
336 structure determination grows faster towards the limit of observed diffraction. Another aspect
337 to be considered is that X-rays and electrons probe different properties of matter,
338 respectively the electron density and the integrated Coulomb potential. Our results prompt
339 a more detailed investigation of these effects and how they affect the representation of
340 features at high resolution.

341 Finally, we noticed that radiation damage can partially explain the shorter distance observed
342 between the nickel atoms in the active site. Given that ions and charged residues are
343 damaged very early on in the exposure (Yano *et al.*, 2005; Hattne *et al.*, 2018), this effect
344 cannot be neglected in structures derived from cryo-EM reconstructions. Novel direct
345 electron detectors with higher frame rates may allow time-resolved experiments to
346 investigate these effects in more detail.

347 Data availability

348 The model has been deposited at the PDB under accession code 6YL3. The map has been
349 deposited at the EMDB under accession code EMD-10835. Raw electron microscopy data

350 is deposited in EMPIAR, accession code EMPIAR-10389.

351 Acknowledgments

352 The authors would like to thank L. Kovacik and K. Goldie for assistance in data collection
353 and S. Klumpe, A. Nunes-Alves, R. Ligabue-Braun and T. Nakane for discussions. Cryo-EM
354 data processing calculations were performed at sciCORE (http://scicore.unibas.ch/)
355 scientific computing center at the University of Basel. R.D.R. and L.A. acknowledge funding
356 from the Fellowships for Excellence program sponsored by the Werner-Siemens Foundation
357 and the University of Basel. This work was in part supported by the Swiss National Science
358 Foundation (grants 177195 and 185544, NCCR TransCure).

359 Author Contributions

360 R.D.R. and R.A. performed the cryo-EM experiments and data analysis. L.A. built and
361 analyzed the atomic model. R.P.J. performed X-ray crystallography experiments. M.A.M.
362 expressed and purified the protein. P.R. prepared and screened EM samples. J.Z.
363 performed the higher-order aberration corrections and analysis. T.S., T.M. and H.S. initiated
364 and supervised the project. R.D.R, L.A., R.A., T.M. and H.S. wrote the manuscript with
365 assistance from all authors.

366 Methods

367 *Protein expression and purification*

368 The *Y. enterocolitica* urease was purified for cryo-electron microscopy according to the
369 protocol of (Rokita *et al.*, 2000). The strain was precultured overnight at 37°C for 18 hours
370 in a medium containing 37 g/l of brain/heart infusion (Oxoid, CM0225), 50 µg/ml
371 streptomycin sulfate (Applichem, A1852.0100), 35 µg/ml nalidixic acid (Applichem,
372 A1894.0025), 50 µg/ml meso-diaminopimelic acid (Sigma, D1377) and 100 µM nickel(II)

373 chloride hexahydrate (Sigma, N6136). 6 x 600ml of expression cultures were inoculated at
374 OD of 1 at 28°C for 23 hours. Cells were harvested by centrifugation and the cell pellet
375 resuspended in 0.15M NaCl, 50mM Tris pH 8.0. The cell lysate was applied directly to a
376 Sephacryl S-300 HR 26/60 column equilibrated with 150 mM NaCl, 50mM TrisHCl pH 8.0.
377 The active fractions as identified by a phenol-hypochlorite assay (Weatherburn, 1967) were
378 buffer-exchanged to 50mM Tris pH 7.0 within a centrifugal filter unit (Sartorius, Vivaspin
379 MWCO 50kDa) and applied to a Mono Q HR 5/5 column pre-equilibrated with 50mM
380 TrisHCl, pH 7.0. The protein was eluted in 50mM Tris pH 7.0 by a gradient to 1M NaCl,
381 concentrated on a centrifugal filter unit (Sartorius, Vivaspin MWCO 50 kDa) and purified by
382 SEC as before. The purity of the urease sample of the two preparations was verified on a
383 4%/12% SDS-PAGE and by mass spectroscopy.

384 *Sample preparation*

385 Approximately 3 µl of the 0.39 mg/ml urease solution were applied to glow-discharged
386 Quantifoil holey carbon grids. After 3-second blotting, the grids were flash-frozen in liquid
387 ethane, using a FEI Vitrobot IV (Thermo Fisher Scientific) with the environmental chamber
388 set at 90% humidity and 20 °C temperature.

389 *Data acquisition*

390 Cryo-EM data were collected on a FEI Titan Krios (Thermo Fisher Scientific) transmission
391 electron microscope, operated at 300 kV and equipped with a Quantum-LS imaging energy
392 filter (GIF, 20 eV zero loss energy window; Gatan Inc.) and a K2 Summit direct electron
393 detector (Gatan Inc.) operated in dose fractionation mode. Data acquisition was controlled
394 by the SerialEM (Schorb *et al.*, 2019) software, performed in counting mode, with a 42 $e^-/Å^2$
395 total exposure fractioned into 40 frames over 8 seconds. The physical pixel size was 0.639
396 Å at the sample level. The data was pre-processed via the FOCUS package (Biyani *et al.*,
397 2017), including drift-correction and dose-weighting using MotionCor2 (Zheng *et al.*, 2017)

398 (grouping every 5 frames and using 3x3 tiles) and CTF estimation using CTFFIND4 (Rohou
399 & Grigorieff, 2015) (using information between 30 Å and 5 Å from the movie stacks). With
400 these settings, we collected two datasets: one using beam-image shift (Cheng *et al.*, 2018),
401 with three shots per grid hole, comprising 2,243 movies, and a second one taking a single
402 shot per hole, with 2,252 movies. A summary of data collection information is given in the
403 **Supp. Tab. 1**.

404 *Image processing*

405 The two datasets were initially processed separately as shown in the flowchart of **Supp. Fig.**
406 **2**. We excluded all movies whose resolution of CTF fitting was worse than 4 Å according to
407 CTFFIND4, leaving 2,197 movies in the multi-shot dataset or 2,115 in the single-shot dataset
408 for further processing. Using the template-free LoG-picker algorithm (Zivanov *et al.*, 2018)
409 we picked an initial set of 157,699 particle coordinates on the multi-shot dataset. These
410 particles were extracted and subjected to one round of 2D classification with the aim of
411 removing "bad" or false-positive particles. Best results in 2D classification were observed
412 when enabling the RELION option "Ignore CTFs until first peak?". Selecting only the classes
413 displaying views of urease with high resolution features, a new subset containing 60,271
414 particles was obtained. Using this subset, a first 3D map was obtained by the *ab initio*
415 stochastic gradient descent (SGD) algorithm (Zivanov *et al.*, 2018; Punjani *et al.*, 2017) with
416 and without tetrahedral symmetry imposed. The symmetric map was consistent with
417 previously determined structures of ureases (Arnold *et al.*, 2016; Ha *et al.*, 2001). The
418 particles were then subjected to 3D refinement using the map from the *ab initio* procedure
419 as starting reference, resulting in a map at 2.6 Å resolution. We then generated new
420 templates for particle picking by low-pass filtering the unsharpened map from this first 3D
421 refinement to 20 Å and calculating evenly oriented 2D projections from it. These templates
422 were then used for picking with Gautomatch (K. Zhang, http://www.mrc-
423 lmb.cam.ac.uk/kzhang/), detecting 107,399 particle coordinates on the multi-shot dataset or

424 87,204 particle coordinates on the single-shot dataset. Visual inspection of randomly
425 selected micrographs indicated this set of coordinates was better than that previously found
426 by the LoG-picker, in the sense that it contained fewer false positives and more true
427 particles. The newly extracted particles were then subjected to 2D and 3D classification
428 procedures to get rid of false positive, damaged or broken particles, which yielded cleaner
429 subsets with 62,884 (multi-shot) or 51,173 (single-shot) particles. Using the current best
430 map from the multi-shot dataset as a starting reference, we then performed masked 3D
431 refinements on the two datasets separately, interleaved with rounds of CTF refinement and
432 Bayesian particle polishing (Zivanov *et al.*, 2019*a*). More specifically, we refined defocus *per*
433 *particle*, astigmatism *per micrograph* and beam tilt *globally* in CTF refinement. In the multi-
434 shot dataset, each of the three relative "shooting targets" were assigned a different class for
435 separate beam tilt refinement. The parameters for Bayesian particle polishing were trained
436 separately on ~5,000 particles from each dataset at this stage. Each dataset yielded refined
437 maps at 2.10 Å (multi-shot) and 2.20 Å (single-shot) resolution. Best results, however, were
438 obtained when merging the particles picked by template-matching on each dataset (194,603
439 particles in total) and processing them altogether. After 2D classification, 141,069 particles
440 remained **(Supp. Fig. 1b),** and after 3D classification, there were 119,020 particles
441 **(Supp. Fig. 1c)**. CTF refinement was then performed using four beam tilt classes, with the
442 particles from the single-shot dataset belonging to a new, fourth class **(Supp. Tab. 2)**.
443 Defocus and astigmatism were both refined *per particle* this time, resulting in a map
444 resolution of 2.05 Å. We compared polishing the full merged dataset at once and each beam
445 tilt class separately, to verify if there were differences in the patterns of particle motion. For
446 training the polishing parameters ~10,000 particles were used in each case this time.
447 Although we did observe different statistics of particle motion **(Supp. Tab. 3)**, resolution and
448 overall quality of the map did not improve further by performing either merged or separate
449 polishing of the different shots. Finally, correction of third-order aberrations in RELION-3.1

450 (Zivanov *et al.*, 2019*b*) **(Supp. Fig. 3)** followed by local 3D refinement resulted in a global
451 map resolution of 1.98 Å. The angular distribution efficiency was estimated using the
452 program cryoEF (Naydenova & Russo, 2017).

453 All resolution estimates reported were obtained by considering the 0.143 threshold
454 (Rosenthal & Henderson, 2003) on the Fourier shell correlation (FSC) curve (Harauz & van
455 Heel, 1986) between independently refined half-maps (Scheres & Chen, 2012). A solvent-
456 excluding mask was generated by low-pass filtering the maps to 12 Å, binarizing the filtered
457 map and adding a soft edge consisting of a cosine-shaped falloff to zero. The FSC curve
458 was corrected for artificial correlations introduced by the mask (Chen *et al.*, 2013). Local
459 resolution was estimated using the approach implemented in RELION
460 (Cardone *et al.*, 2013).

461 *Model building, refinement and analysis*

462 After refinement of the map to high resolution it had to be flipped in UCSF Chimera
463 (Pettersen *et al.*, 2004) to match the correct handedness. The biological assembly from the
464 crystal structure of *Y. enterocolitica* urease **(Supp. Note 1)** was rigid-body fitted to the map
465 in Chimera. The non-crystallographic symmetry (NCS) was calculated with PHENIX v1.17
466 (Adams *et al.*, 2002) from the crystal structure. Only using the hetero-trimer of the three
467 proteins, backbone and side chains were built, corrected or confirmed in Coot (Emsley &
468 Cowtan, 2004). After several rounds of manual refinement of the model in Coot, applying
469 NCS and real-space refinement in PHENIX, the model comprised side chains of residues 1-
470 100 of ureA, 31-162 of ureB and 2-327, 335-572 of ureC. Residues 328-334 are disordered
471 and could not be modeled with confidence. NCS constraints were not used during final
472 refinements as to include alternative side chain conformations. Waters were built manually
473 and refined in PHENIX and were added to the closest chain by the program
474 phenix.sort_hetatoms. The quality of the refinement was assessed by cryo-EM Validation
475 tool **(Table 1)** (Afonine, Klaholz *et al.*, 2018).

476

477 *Structure analysis*

478 The electrostatic potential was calculated using the APBS plugin in PyMOL (Jurrus et al,
479 2018). The ConSurf server (Berezin *et al.*, 2004; Ashkenazy *et al.*, 2016) was used to find
480 150 sequences per urease protein for alignment with ClustalW (Madeira *et al.*, 2019) and
481 calculate conservation per residue. The "sample the list of homologs" option was used to
482 get a diverse representation across all species. The sequence identity of the 150 sequences
483 was determined using BLSM62 in Geneious (Kearse *et al.*, 2012). The PDBePISA server
484 (https://www.ebi.ac.uk/pdbe/pisa/) was used to find and calculate interface areas (Krissinel
485 & Henrick, 2007). Figures were created using UCSF Chimera (Pettersen *et al.*, 2004),
486 ChimeraX (Goddard *et al.*, 2018), PyMol (Schrödinger), Inkscape, Adobe Illustrator and
487 Adobe Photoshop.

488

489 *Radiation damage analysis*

490 Bayesian particle polishing in RELION (Zivanov *et al.*, 2019*a*, 2018) was carried out on a
491 sliding-window basis along the exposure, including 5 frames at a time, starting from frame
492 1 up to frame 25. Half-set reconstructions were then created from each polished particle
493 stack and post-processed using the same mask as that applied to the reconstruction from
494 all frames. On each post-processed reconstruction, real space refinement of chain C (α-
495 subunit containing the active site) from the full reconstruction was carried out in PHENIX
496 (Afonine, Poon *et al.*, 2018) for 5 macro-cycles. This procedure was repeated 5 times with
497 different random seeds. Distance between residues in the resulting refined models were
498 calculated using BioPython (Cock *et al.*, 2009) and plotted using the NumPy
499 (https://www.numpy.org) and Matplotlib (https://www.matplotlib.org) Python modules.

500 **References**

501 Adams, P. D., Grosse-Kunstleve, R. W., Hung, L.-W., Ioerger, T. R., McCoy, A. J., Moriarty, N. W., Read, R.
502 J., Sacchettini, J. C., Sauter, N. K. & Terwilliger, T. C. (2002). *Acta Crystallogr. Sect. D*. **58**, 1948–1954.

503 Afonine, P. V, Klaholz, B. P., Moriarty, N. W., Poon, B. K., Sobolev, O. V, Terwilliger, T. C., Adams, P. D. &
504 Urzhumtsev, A. (2018). *Acta Crystallogr. Sect. D Struct. Biol.* **74**, 814–840.

505 Afonine, P. V, Poon, B. K., Read, R. J., Sobolev, O. V, Terwilliger, T. C., Urzhumtsev, A. & Adams, P. D.
506 (2018). *Acta Crystallogr. Sect. D*. **74**, 531–544.

507 Arnold, S. A., Albiez, S., Bieri, A., Syntychaki, A., Adaixo, R., Mcleod, R. A., Goldie, K. N., Stahlberg, H. &
508 Braun, T. (2016). *J. Struct. Biol.* **197**, 0–6.

509 Ashkenazy, H., Abadi, S., Martz, E., Chay, O., Mayrose, I., Pupko, T. & Ben-Tal, N. (2016). *Nucleic Acids*
510 *Res.* **44**, W344–W350.

511 Benini, S., Rypniewski, W. R., Wilson, K. S., Ciurli, S. & Mangani, S. (1998). *JBIC J. Biol. Inorg. Chem.* **3**,
512 268–273.

513 Berezin, C., Glaser, F., Rosenberg, J., Paz, I., Pupko, T., Fariselli, P., Casadio, R. & Ben-Tal, N. (2004).
514 *Bioinformatics*. **20**, 1322–1324.

515 Biyani, N., Righetto, R. D., McLeod, R., Caujolle-Bert, D., Castano-Diez, D., Goldie, K. N. & Stahlberg, H.
516 (2017). *J. Struct. Biol.* **198**, 124–133.

517 Blanc, E., Roversi, P., Vonrhein, C., Flensburg, C., Lea, S. M. & Bricogne, G. (2004). *Acta Crystallogr. Sect.*
518 *D Biol. Crystallogr.* **60**, 2210–2221.

519 Brilot, A. F., Chen, J. Z., Cheng, A., Pan, J., Harrison, S. C., Potter, C. S., Carragher, B., Henderson, R. &
520 Grigorieff, N. (2012). *J. Struct. Biol.* **177**, 630–637.

521 Cardone, G., Heymann, J. B. & Steven, A. C. (2013). *J. Struct. Biol.* **184**, 226–236.

522 Chen, S., McMullan, G., Faruqi, A. R., Murshudov, G. N., Short, J. M., Scheres, S. H. W. & Henderson, R.
523 (2013). *Ultramicroscopy*. **135**, 24–35.

524 Cheng, A., Eng, E. T., Alink, L., Rice, W. J., Jordan, K. D., Kim, L. Y., Potter, C. S. & Carragher, B. (2018). *J.*
525 *Struct. Biol.* **204**, 270–275.

526 Cock, P. J. A., Antao, T., Chang, J. T., Chapman, B. A., Cox, C. J., Dalke, A., Friedberg, I., Hamelryck, T.,
527 Kauff, F., Wilczynski, B. & de Hoon, M. J. L. (2009). *Bioinformatics*. **25**, 1422–1423.

528 Dixon, N. E., Gazzola, C., Blakeley, R. L. & Zerner, B. (1975). *J. Am. Chem. Soc.* **97**, 4131–4133.

529 Drummond, N., Murphy, B. P., Ringwood, T., Prentice, M. B., Buckley, J. F. & Fanning, S. (2012). *Foodborne*
530 *Pathog. Dis.* **9**, 179–189.

531 Emsley, P. & Cowtan, K. (2004). *Acta Crystallogr. Sect. D*. **60**, 2126–2132.

532 Fromm, S. A., Bharat, T. A. M., Jakobi, A. J., Hagen, W. J. H. & Sachse, C. (2015). *J. Struct. Biol.* **189**, 87–
533 97.

534 Goddard, T. D., Huang, C. C., Meng, E. C., Pettersen, E. F., Couch, G. S., Morris, J. H. & Ferrin, T. E.
535 (2018). *Protein Sci.* **27**, 14–25.

536 Grant, T. & Grigorieff, N. (2015). *Elife*. **4**,.

537 Gripenberg-Lerche, C., Zhang, L., Ahtonen, P., Toivanen, P. & Skurnik, M. (2000). *Infect. Immun.* **68**, 942–
538 947.

539 Ha, N.-C., Oh, S.-T., Sung, J. Y., Cha, K. A., Lee, M. H. & Oh, B.-H. (2001). *Nat. Struct. Biol.* **8**, 505.

540 Harauz, G. & van Heel, M. (1986). *Optik (Stuttg).* **78**, 146–156.

541 Hattne, J., Shi, D., Glynn, C., Zee, C., Gallagher-Jones, M., Martynowycz, M. W., Rodriguez, J. A. & Gonen,
542 T. (2018). *Structure*. **26**, 759-766.e4.

543 Jabri, E., Carr, M., Hausinger, R. & Karplus, P. (1995). *Science (80-.).* **268**, 998–1004.

544 Kappaun, K., Regina, A., Regina, C. & Ligabue-braun, R. (2018). *J. Adv. Res.* **13**, 3–17.

545 Kearse, M., Moir, R., Wilson, A., Stones-Havas, S., Cheung, M., Sturrock, S., Buxton, S., Cooper, A.,
546 Markowitz, S., Duran, C., Thierer, T., Ashton, B., Meintjes, P. & Drummond, A. (2012). *Bioinformatics*.
547 **28**, 1647–1649.

548 Krissinel, E. & Henrick, K. (2007). *J. Mol. Biol.* **372**, 774–797.

549 Ligabue-Braun, R., Andreis, F. C., Verli, H. & Carlini, C. R. (2013). *Naturwissenschaften*. **100**, 459–467.

550 Madeira, F., Park, Y. M., Lee, J., Buso, N., Gur, T., Madhusoodanan, N., Basutkar, P., Tivey, A. R. N.,
551 Potter, S. C., Finn, R. D. & Lopez, R. (2019). *Nucleic Acids Res.* **47**, W636–W641.

552 Maroney, M. J. & Ciurli, S. (2014). *Chem. Rev.* **114**, 4206–4228.

553 Mazzei, L., Cianci, M., Contaldo, U., Musiani, F. & Ciurli, S. (2017). *Biochemistry*. **56**, 5391–5404.

554 McCoy, A. J., Grosse-Kunstleve, R. W., Adams, P. D., Winn, M. D., Storoni, L. C. & Read, R. J. (2007). *J.*
555 *Appl. Crystallogr.* **40**, 658–674.

556 Naydenova, K. & Russo, C. J. (2017). *Nat. Commun.* **8**, 629.

557 Pearson, M. A., Michel, L. O., Hausinger, R. P. & Karplus, P. A. (1997). *Biochemistry*. **36**, 8164–8172.

558 Pettersen, E. F., Goddard, T. D., Huang, C. C., Couch, G. S., Greenblatt, D. M., Meng, E. C. & Ferrin, T. E.
559 (2004). *J. Comput. Chem.* **25**, 1605–1612.

560 Podschun, R. & Ullmann, U. (1998). *Clin. Microbiol. Rev.* **11**, 589–603.

561 Punjani, A., Rubinstein, J. L., Fleet, D. J. & Brubaker, M. A. (2017). *Nat. Methods*. **14**, 290–296.

562 Rohou, A. & Grigorieff, N. (2015). *J. Struct. Biol.* **192**, 216–221.

563 Rokita, E., Makristathis, A., Hirschl, A. M. & Rotter, M. L. (2000). *J. Chromatogr. B Biomed. Sci. Appl.* **737**,
564 203–212.

565 Rosenthal, P. B. & Henderson, R. (2003). *J. Mol. Biol.* **333**, 721–745.

566 Scheres, S. H. W. W. & Chen, S. (2012). *Nat. Methods*. **9**, 853–854.

567 Schorb, M., Haberbosch, I., Hagen, W. J. H., Schwab, Y. & Mastronarde, D. N. (2019). *Nat. Methods*.

568 Sumner, J. B. (1926). *J. Biol. Chem.* **69**, 435–441.

569 Weatherburn, M. W. (1967). *Anal. Chem.* **39**, 971–974.

570 Yano, J., Kern, J., Irrgang, K.-D., Latimer, M. J., Bergmann, U., Glatzel, P., Pushkar, Y., Biesiadka, J., Loll,
571 B., Sauer, K., Messinger, J., Zouni, A. & Yachandra, V. K. (2005). *Proc. Natl. Acad. Sci.* **102**, 12047–
572 12052.

573 Young, G. M., Amid, D. & Miller, V. L. (1996). *J. Bacteriol.* **178**, 6487–6495.

574 Zheng, S. Q., Palovcak, E., Armache, J.-P., Verba, K. A., Cheng, Y. & Agard, D. A. (2017). *Nat. Methods*.
575 **14**, 331–332.

576 Zivanov, J., Nakane, T., Forsberg, B. O., Kimanius, D., Hagen, W. J., Lindahl, E. & Scheres, S. H. (2018).
577 *Elife*. **7**, e42166.

578 Zivanov, J., Nakane, T. & Scheres, S. H. W. (2019*a*). *IUCrJ*. **6**,.

579 Zivanov, J., Nakane, T. & Scheres, S. H. W. (2019*b*). *BioRxiv*. 798066.

580

Figures and legends

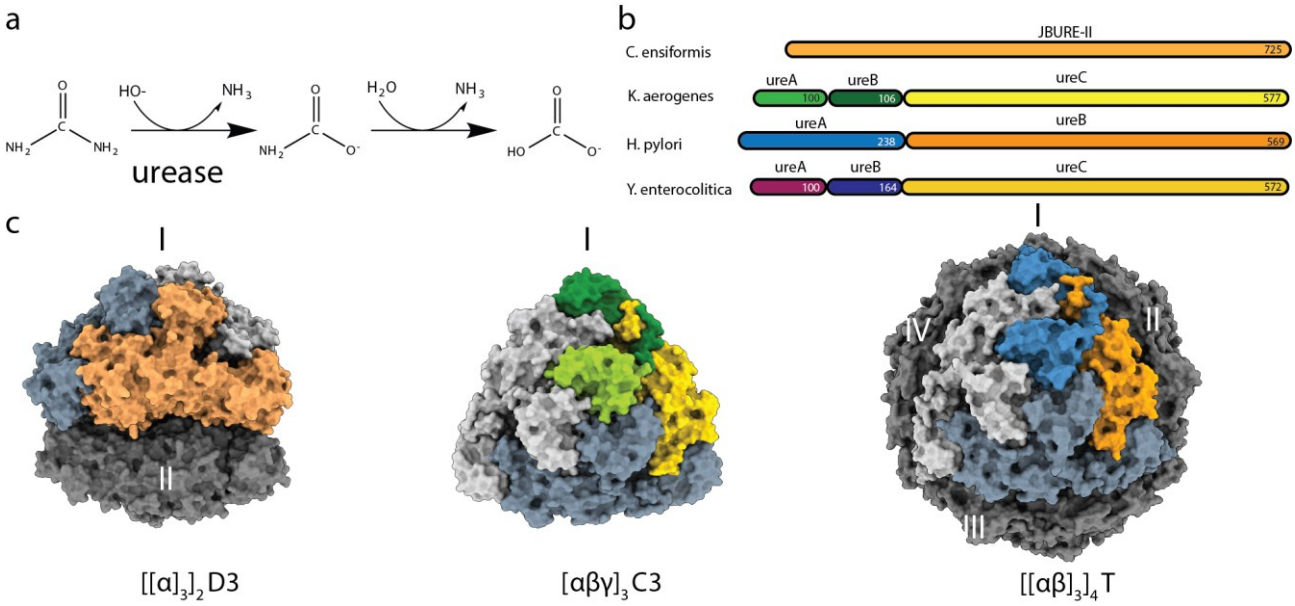

Figure 1 Protein architectures and oligomeric assemblies of ureases. **a)** Schematic of biochemical reaction catalyzed by urease. **b)** Protein architecture of urease functional unit of *C. ensiformis* (Jack bean urease), *K. aerogenes, H. pylori* and *Y. enterocolitica.* **c)** Surface representation of oligomeric assembly of urease in *C. ensiformis* (PDB: 3LA4), *K. aerogenes* (PDB: 1EJW), *H. pylori* (PDB: 1E9Z), respectively. Proteins are color-coded as in **b)**. Oligomeric state of urease assembly is indicated at the bottom and the trimeric assemblies are indicated in roman numerals.

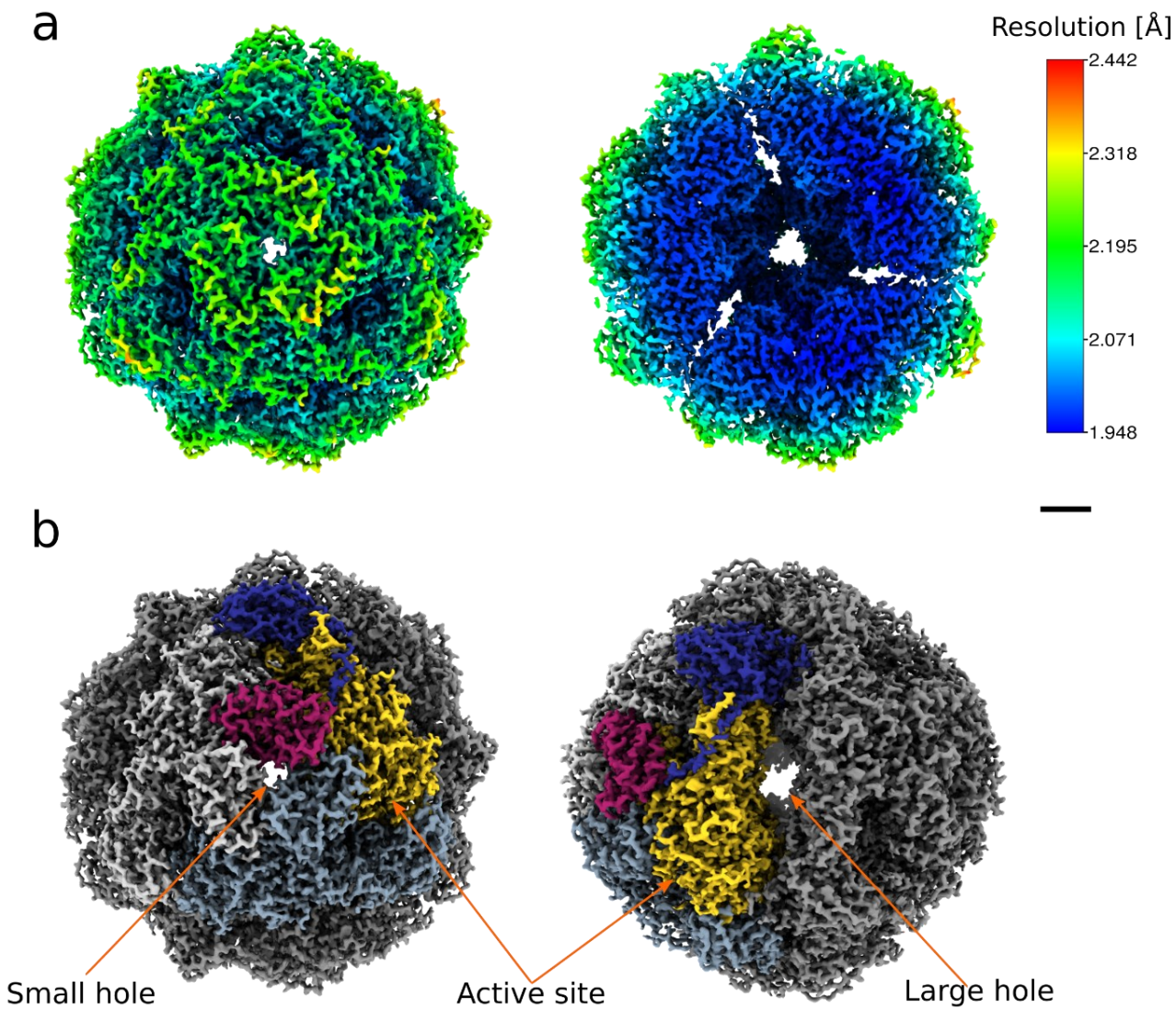

590

591 **Figure 2** Cryo-EM analysis of the *Y. enterocolitica* dodecameric urease assembly. **a)** The
592 cryo-EM map filtered and colored by local resolution (left), and a slice cut through the map
593 to show the internal details (right). **b)** The assembly architecture highlighted on the map.
594 The three chains that form the basic hetero-trimer are shown in different colors, with the
595 other hetero-trimers shown in shades of gray. Two different views are shown to indicate the
596 location of the small and larger holes at the interfaces, as well as the active site.
597 Scale bars: 20 Å.

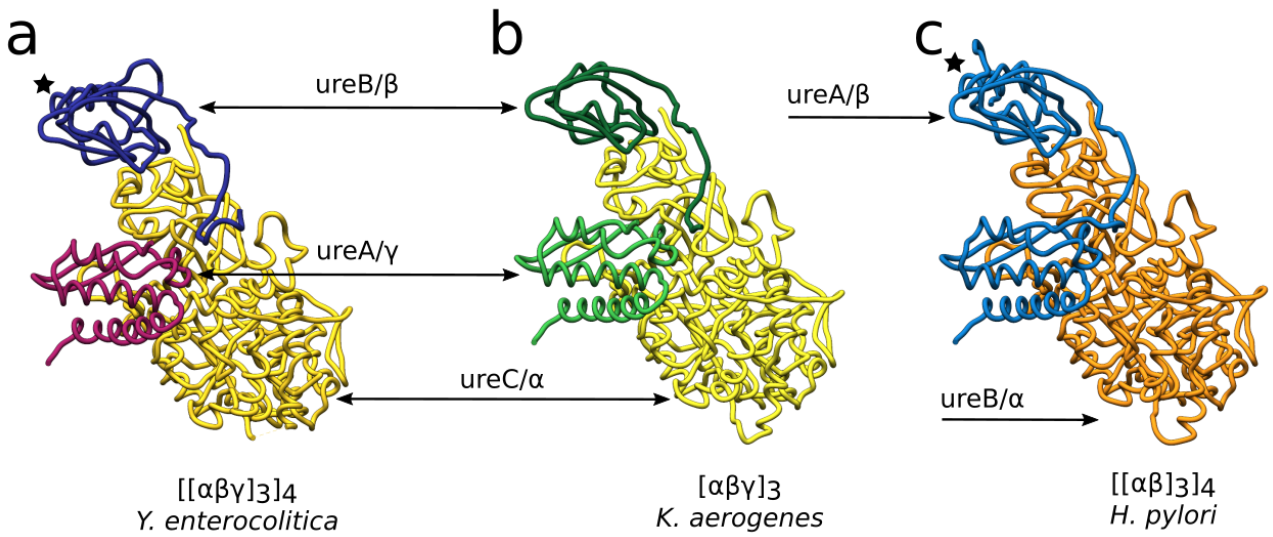

Figure 3 Comparison of *Y. enterocolitica* urease chain architecture with ureases with different modes of assembly from other pathogens. Hetero-trimers are shown in tube representation with each chain in the same colors of the sequences in **Fig. 1b**. The black star indicates the central helix of the β subunit. The *Y. enterocolitica* and *H. pylori* ureases form the same dodecameric assembly despite having different types of chain splitting, while *K. aerogenes* urease has the same type of chain splitting as in *Y. enterocolitica* but forms only a trimeric assembly.

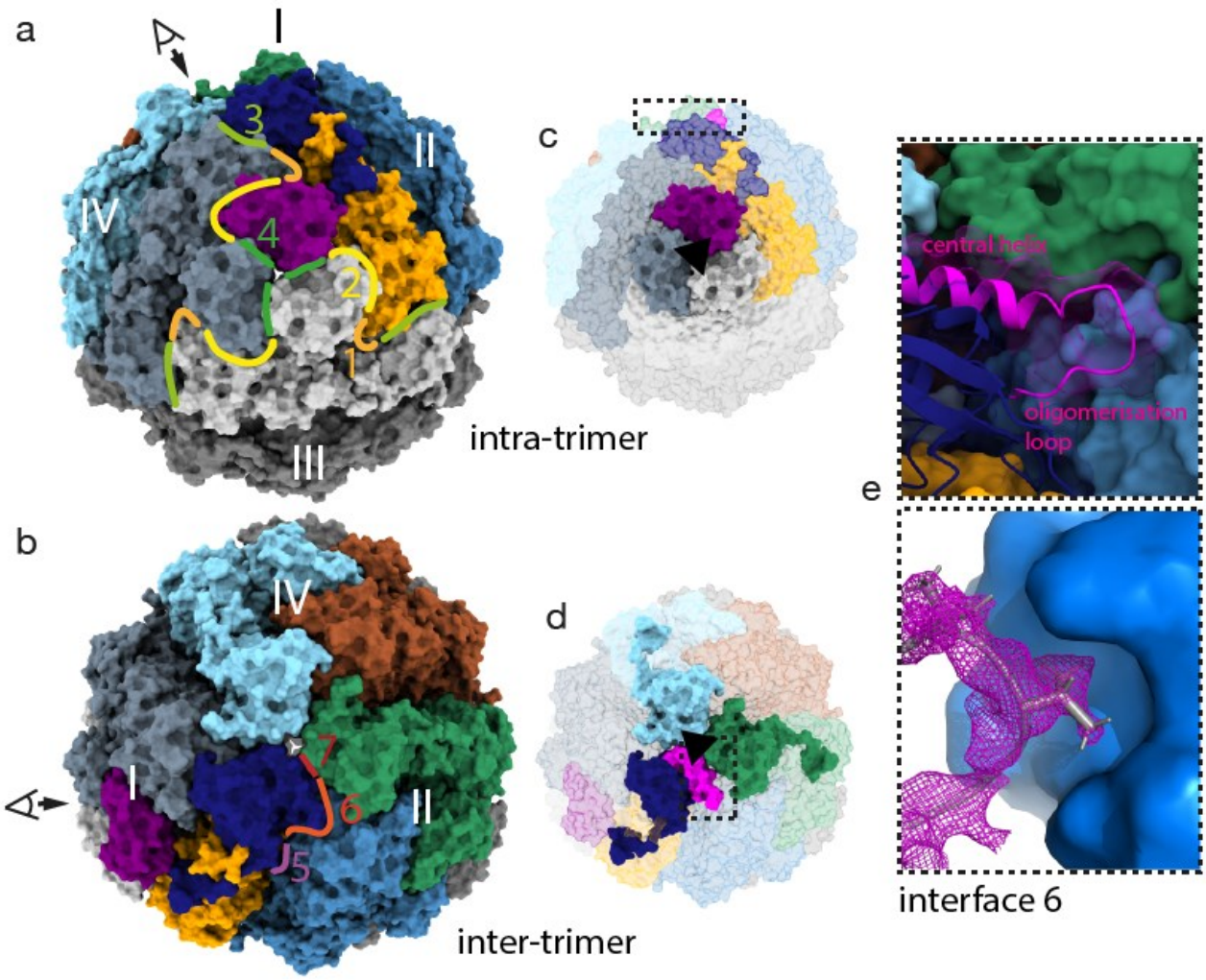

Figure 4 Interfaces in dodecameric assembly of *Y. enterocolitica*. **a)** surface model in front view of trimer of *Y. enterocolitica* urease with intra-trimeric interfaces 1-4 indicated with color-coded lines and numbers. **b)** Same model shown from the top (view indicated with eye) and the inter-trimeric interfaces. **c)** Front view with intra-trimeric-core highlighted and three-fold axis indicated with black triangle. Inset for e) in dashed box. **d)** same as c) but from the top view. **e)** Interface 6 with loop from ureB (magenta) binding into pocket of ureC of neighboring trimer. Upper inset shows ureB in cartoon and transparent surface and ureC in surface representation. Lower panel shows ureC as surface and ureB loop as cartoon with density.

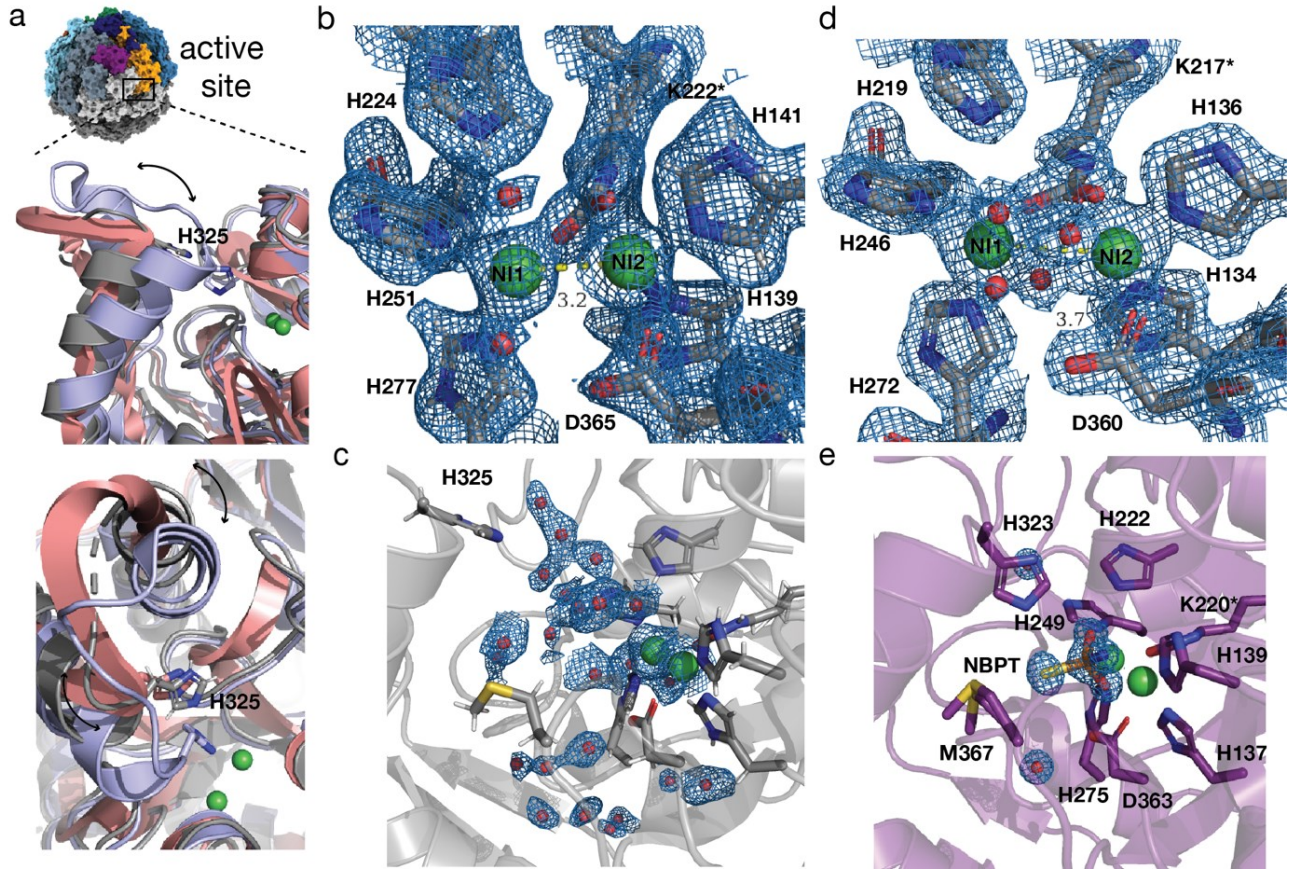

Figure 5 Active site of *Y. enterocolitica* urease. **a)** Overview of urease assembly with the active site location indicated. Inset shows in top panel side view of urease crystal structures from *K. aerogenes* mobile flap shown in open conformation in salmon (PDB: 2UBP) and in closed position as light purple (PDB: 3UBP). In gray the cryo-EM structure of *Y. enterocolitica* is overlaid and the green spheres represent the Ni^{2+} ions of the active site. Bottom panel shows top view of the three structures. Arrows indicate movement of helix and catalytic HIS325 is shown as stick. **b)** Model of active site residues and Ni^{2+} ions with the cryo-EM map of *Y. enterocolitica* at 1.98 Å nominal resolution. Yellow line indicates distance between Ni^{2+} ions in Å; **c)** shows the water molecules in the active site. **d)** Crystal structure of *K. aerogenes* urease at 1.9 Å resolution (PDB: 1EJW). Yellow line indicates distance between Ni^{2+} ions in Å. **e)** Crystal structure of *S. pasteurii* at 1.28 Å with inhibitor NBPT (PDB: 5OL4).

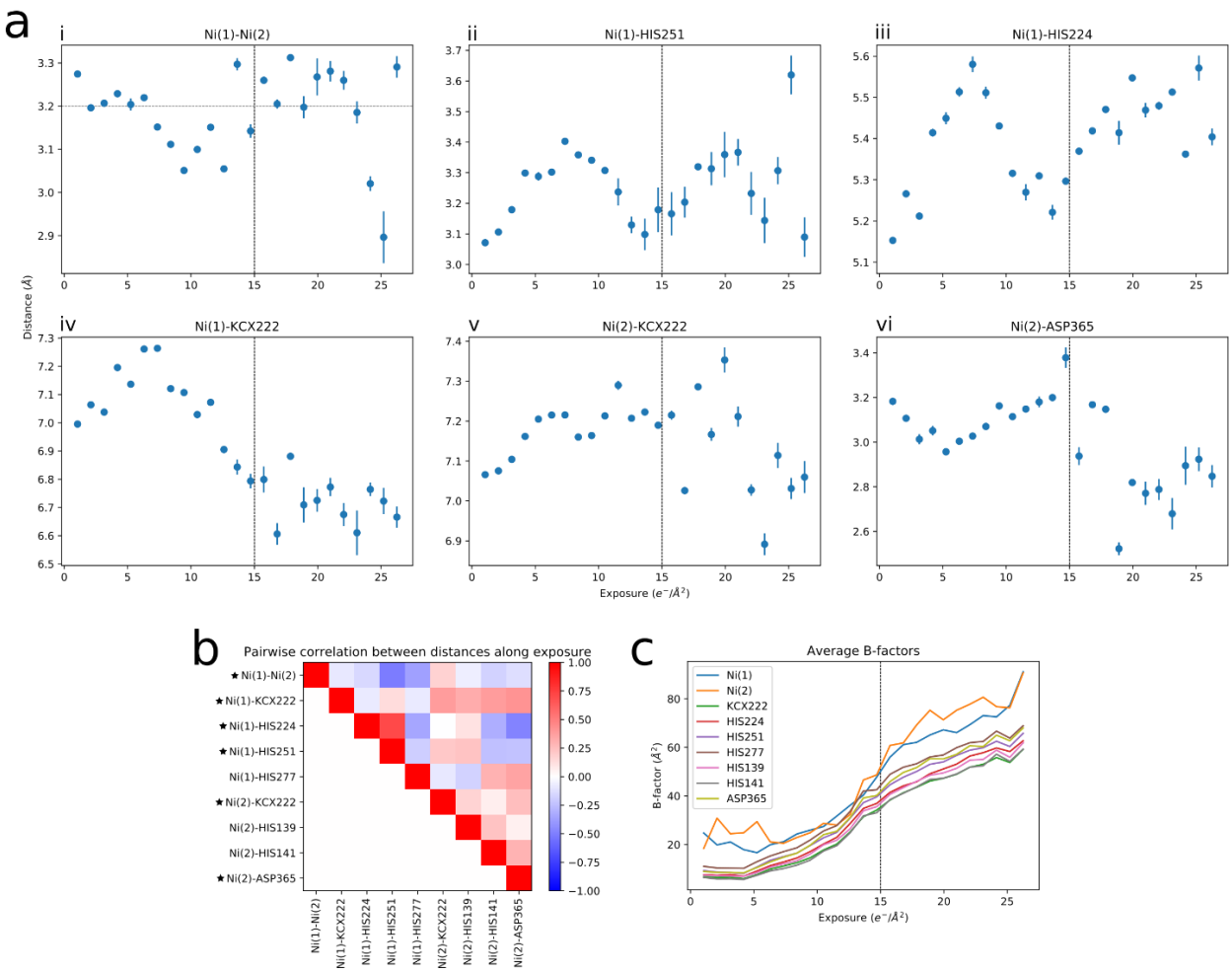

Figure 6 Radiation damage affects the distance between residues in the active site. **a)** Distances between the Ni^{2+} ions and selected residues involved in their coordination are plotted against the accumulated exposure. For each reconstruction calculated along the exposure, the model was refined, and distances measured. Dots indicate the average and error bars show +/- one standard deviation across five refinement runs with different random seeds. Horizontal dashed line in panel a-i) shows the distance in the model obtained from the full reconstruction with all frames. Vertical dashed lines show approximately the exposure at which the density for charged residues completely vanishes (see **Supp. Mov. 2**). **b)** Correlation coefficients between distance changes along the exposure for selected residues involved in ion coordination. Distance plots shown in a) are indicated with a star. **c)** Average B-factors of selected residues plotted against the accumulated exposure.

643 **Table 1** Model building and refinement. Statistics shown for full assembly calculated from

644 the asymmetric unit using NCS.

Model composition	
Chains	36
Non-hydrogen atoms	77076
Protein residues	9552
Waters	3672
Ligands (Ni^{2+})	24
Refinement	
Resolution (Å)	1.98
Average B factor ($Å^2$)	14.45
Rms deviations	
Bonds (Å)	0.066
Angles (°)	3.665
Validation (protein)	
Molprobity score	1.93
Clashscore	4.37
Good rotamers	97.26
Ramachandran plot	
Favored (%)	94.35
Allowed (%)	5.27
Outliers (%)	0.38

645

646 # High-resolution cryo-EM structure of urease from the pathogen

647 # *Yersinia enterocolitica*

648 # *Supplementary Information*

649 **Supplementary Figures**

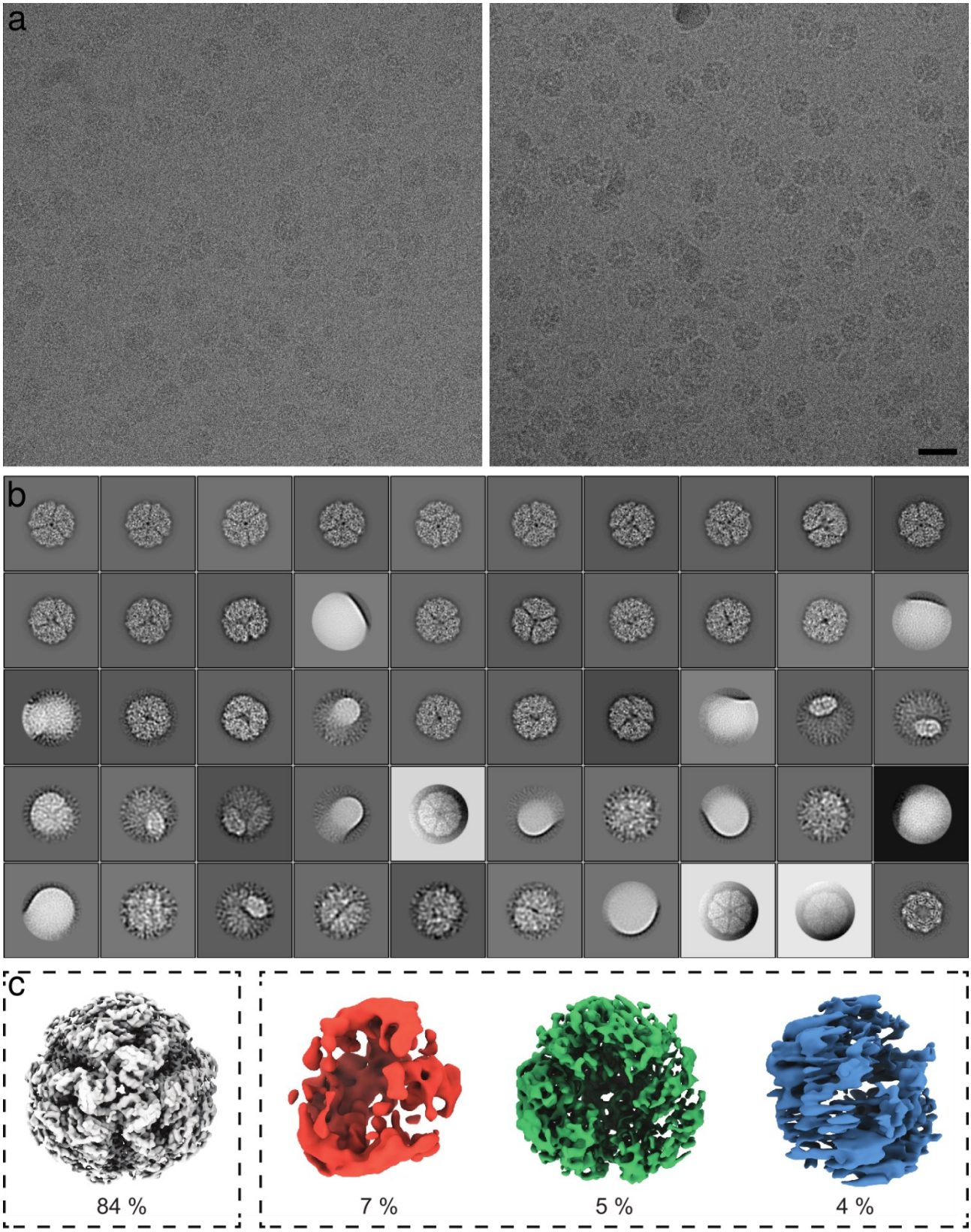

650 Complete Urease Broken Particles / Missing Subunits

651

652 **Supplementary Figure 1** Cryo-EM data of *Y. enterocolitica* urease. **a)** Two representative
653 micrographs from the dataset, acquired at -0.64 and -1.36 µm defocus, respectively. Scale
654 bar: 200 Å. **b)** 2D class averages obtained from 194'603 particles in the merged dataset.
655 These averages were obtained with RELION's "Ignore CTF until first peak" option enabled
656 and are sorted by decreasing order of number of particles in each class. Views of urease
657 with missing subunits are observed. The bottom right average shows a contamination by
658 GroEL. **c)** 3D class averages obtained from 141'069 particles in the merged dataset. These
659 averages were obtained without symmetry imposition in RELION. The 3D classes are sorted
660 by the indicated fraction of particles assigned to it. The first class is a complete dodecameric
661 urease assembly, while the other classes represent urease structures with at least one
662 trimer missing from the tetrahedron.

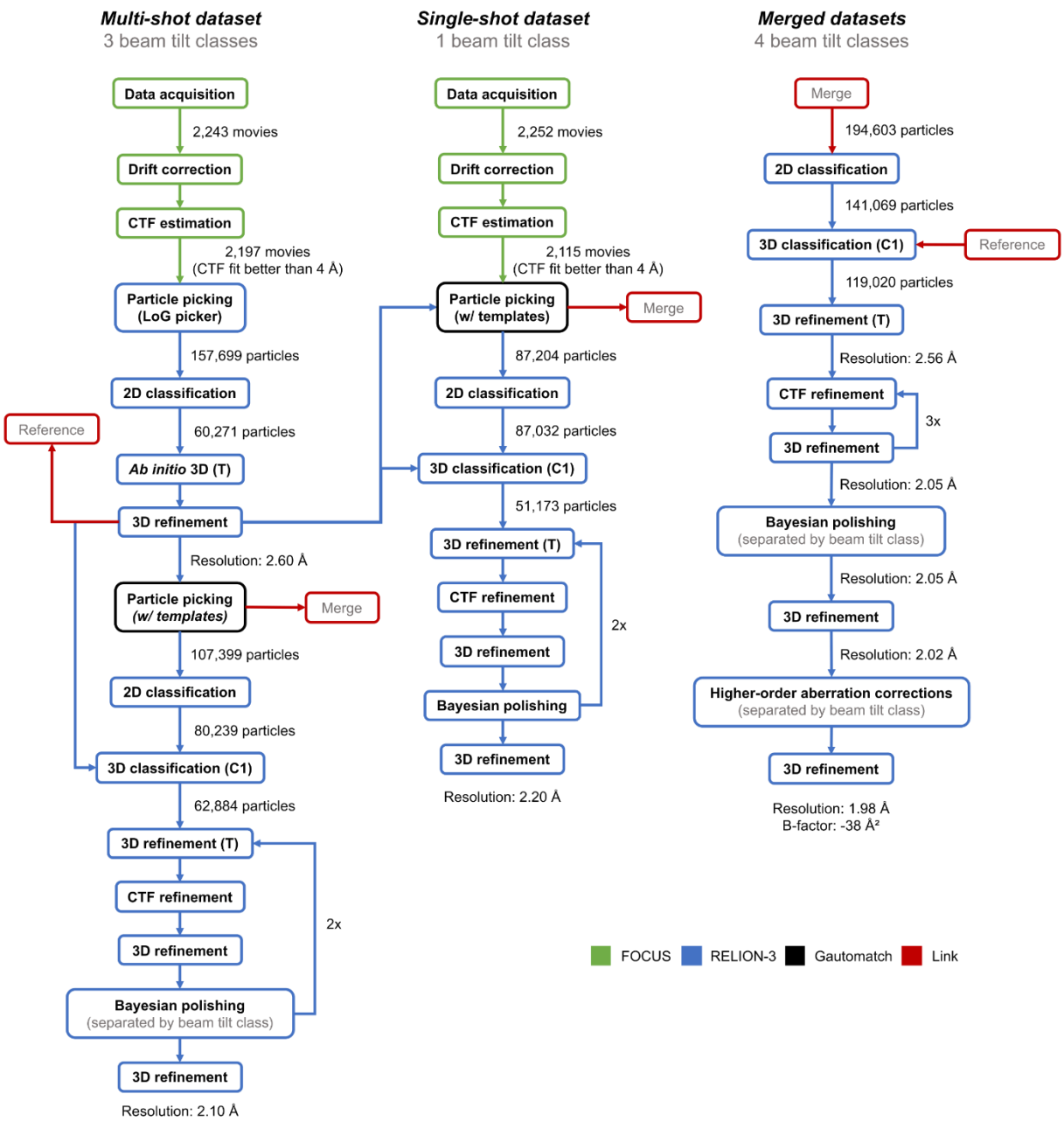

Supplementary Figure 2 Data processing flowchart for the urease cryo-EM map. Masking and postprocessing jobs have been omitted for clarity. All CTF refinement jobs included beam tilt and per-particle defocus refinement (see **Methods** for details). All resolution estimates given correspond to the corrected FSC curves between masked half-maps obtained from postprocessing jobs in RELION.

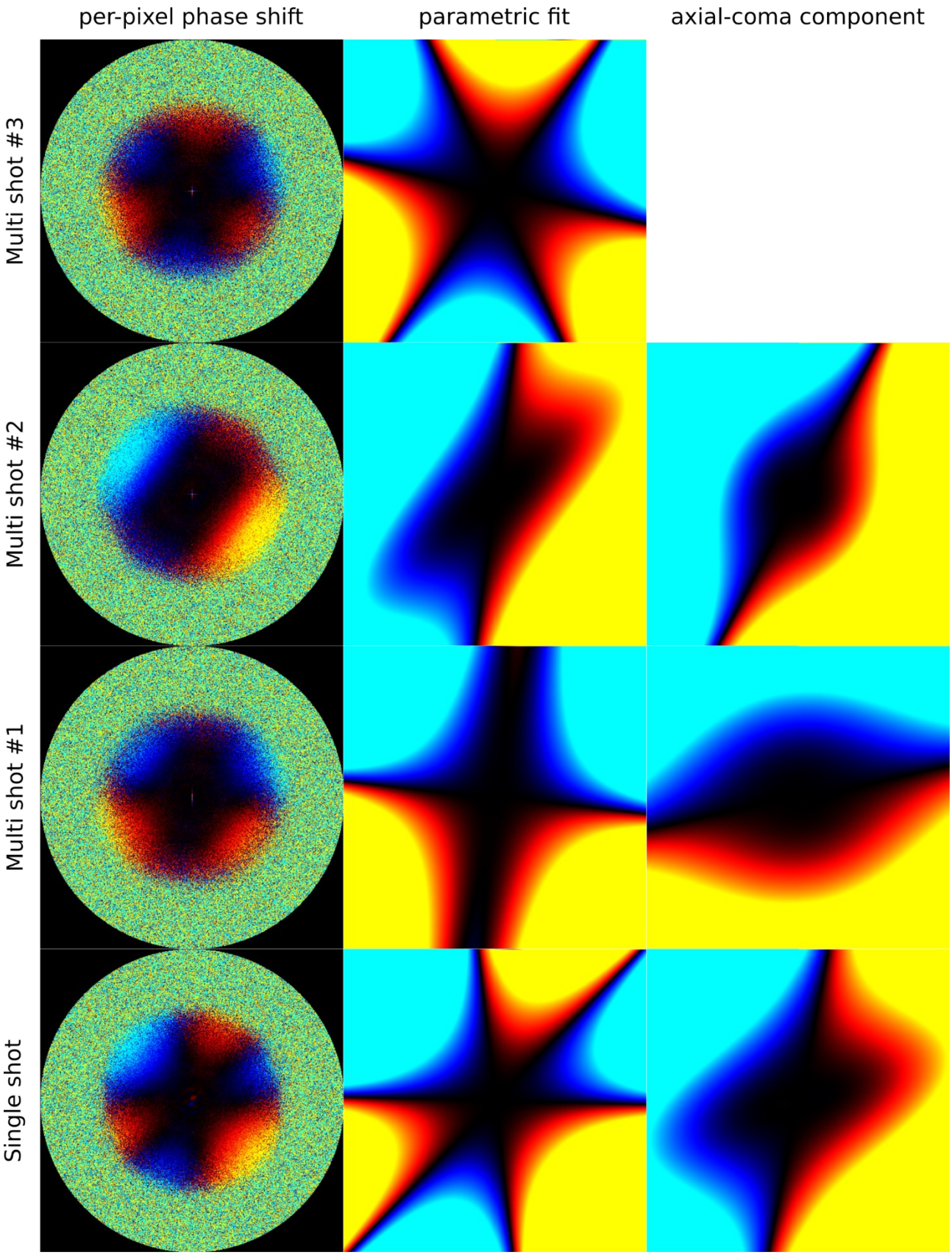
per-pixel phase shift
parametric fit
axial-coma component
Multi shot #3
Multi shot #2
Multi shot #1
Single shot

671 **Supplementary Figure 3** Fits of the anti-symmetrical aberrations arising at the four different
672 beam-shift positions. The left column shows phase shifts measured independently for each
673 Fourier pixel, while the center column shows their parametric fits using third-order Zernike
674 polynomials. The first position (top row, the third beam-shifted multi-shot) corresponds to an
675 essentially untilted beam **(Supp. Tab. 2)**, while the other two multishots and the single-shot
676 dataset exhibit tilts to different extents. Note that even the untilted dataset shows a
677 significant trefoil aberration. In the right column, the parametric fit of the first position has
678 been subtracted, yielding residuals roughly consistent with the axial coma produced by a
679 tilted beam.

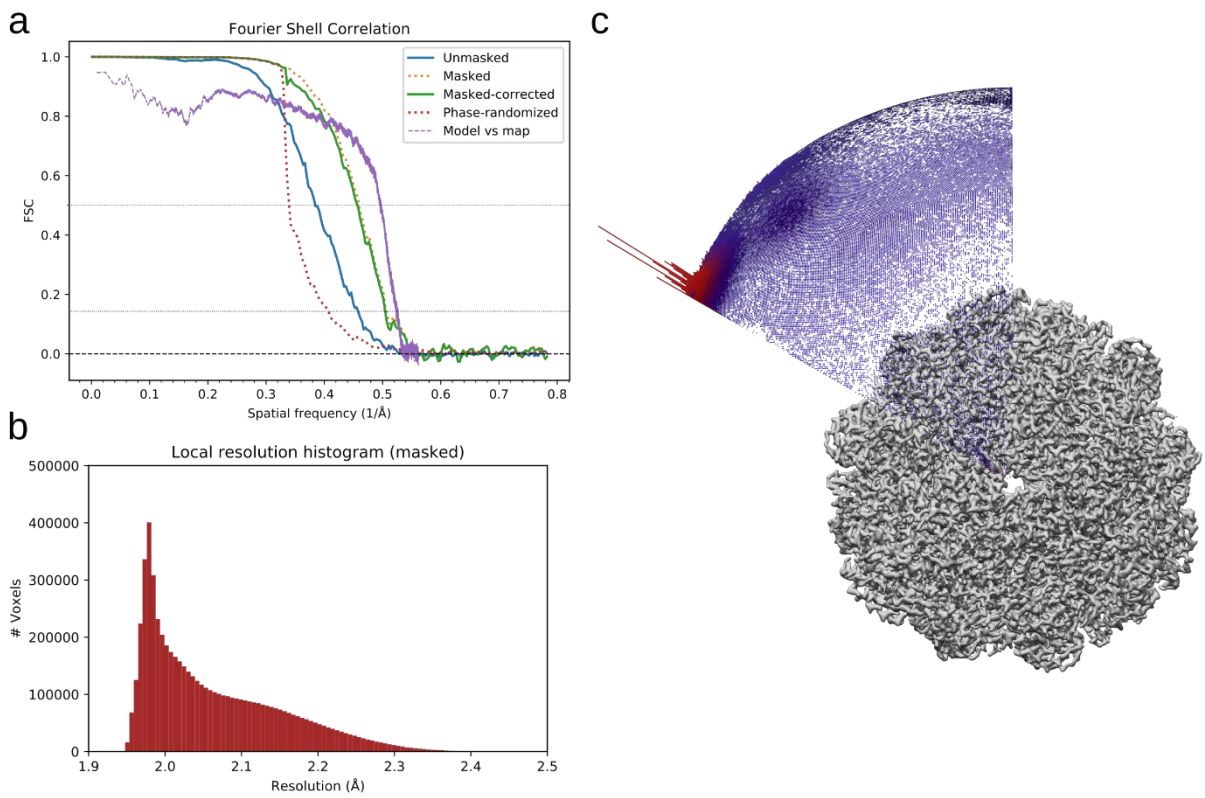

Supplementary Figure 4 Resolution estimates of the urease cryo-EM map. **a)** FSC curves between the half-maps when unmasked (solid blue line), masked (dashed orange), corrected by high-resolution noise substitution after masking (solid green), phase-randomized (dashed red) and between the atomic model and the full experimental map (dashed violet). **b)** Histogram of local resolution assigned to each voxel. **c)** Angular distribution of particles in the urease cryo-EM reconstruction overlaid on the unsharpened map.

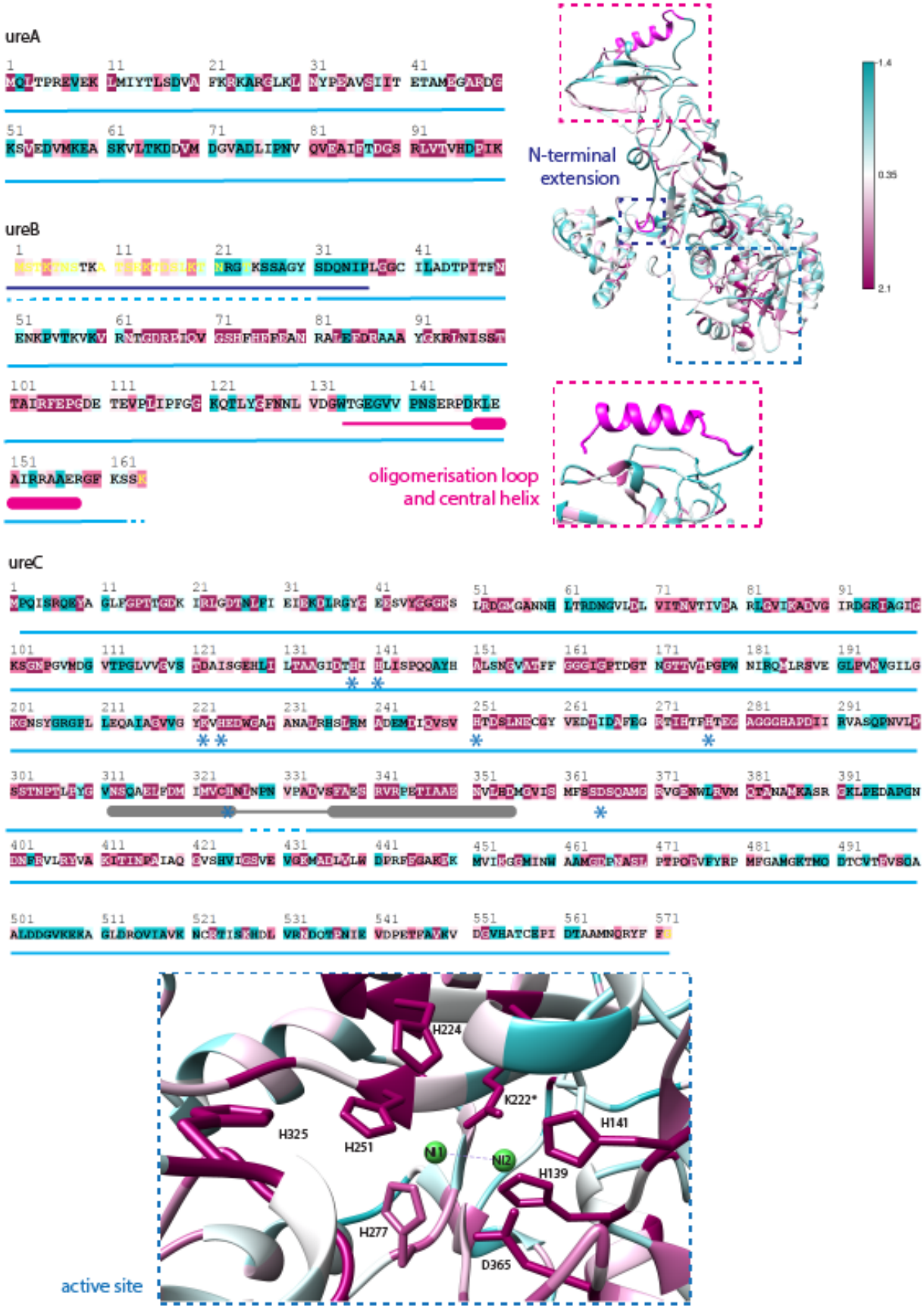
ureA
ureB
ureC
N-terminal extension
oligomerisation loop and central helix
active site
H224
K222*
H141
H325
H251
Ni1
Ni2
H139
H277
D365

688

689

690 **Supplementary Figure 5** Alignment of 150 ureA, ureB and ureC sequences, chosen by
691 sampling from all homologs found for each protein. ClustalW was used for sequence
692 alignment and the ConSurf server for conservation analysis. Conservation is shown on a
693 gradient from dark purple to white to turquoise (arbitrary units). The light blue bar indicates
694 model completeness. Regions of interest are highlighted: The N-terminal extension in dark
695 blue, the oligomerization loop and its following helix are indicated in magenta, the mobile
696 flap is indicated in grey and the blue asterix indicates residues belonging to the active site.
697

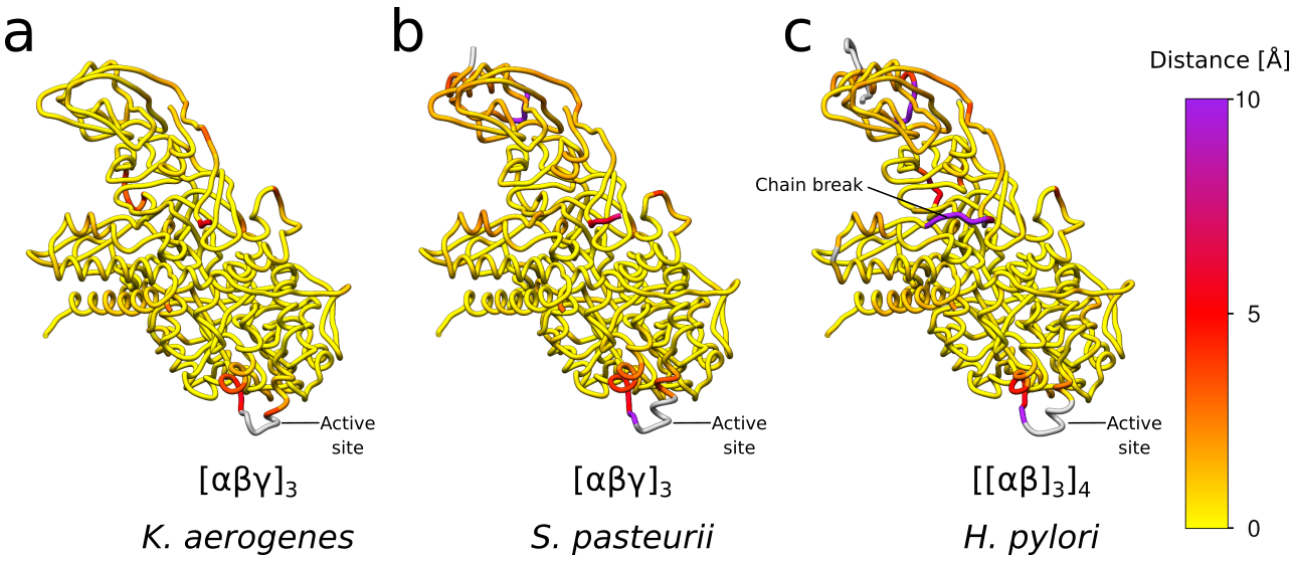

Supplementary Figure 6 Distance comparison between residues of *Y. enterocolitica* urease against ureases with different modes of assembly. Tubes are colored by the pairwise distance of Cα atoms to the corresponding residue in *Y. enterocolitica* urease. Residues without equivalence after sequence alignment are shown in gray color. Segments with particularly high deviations are indicated.

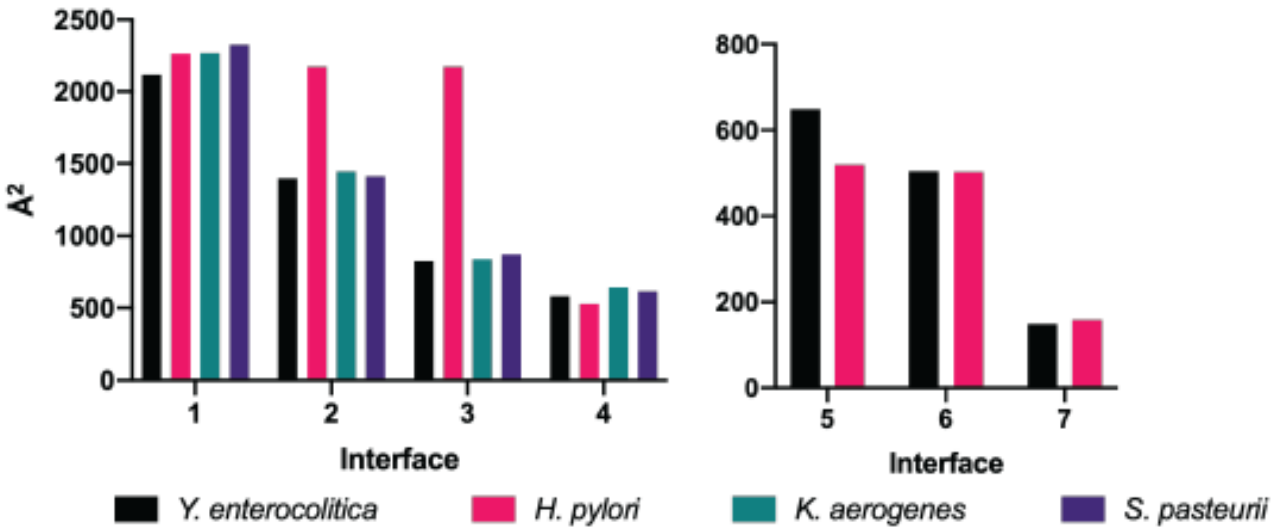

Supplementary Figure 7 Area (Å^2) of interfaces 1-7 (numbering as in Figure 4) plotted by organism. Left: intra-trimer interfaces; right: inter-trimer interfaces. The intra-trimer areas of interfaces 2 and 3 in *H. pylori* are higher because they are part of the same chain.

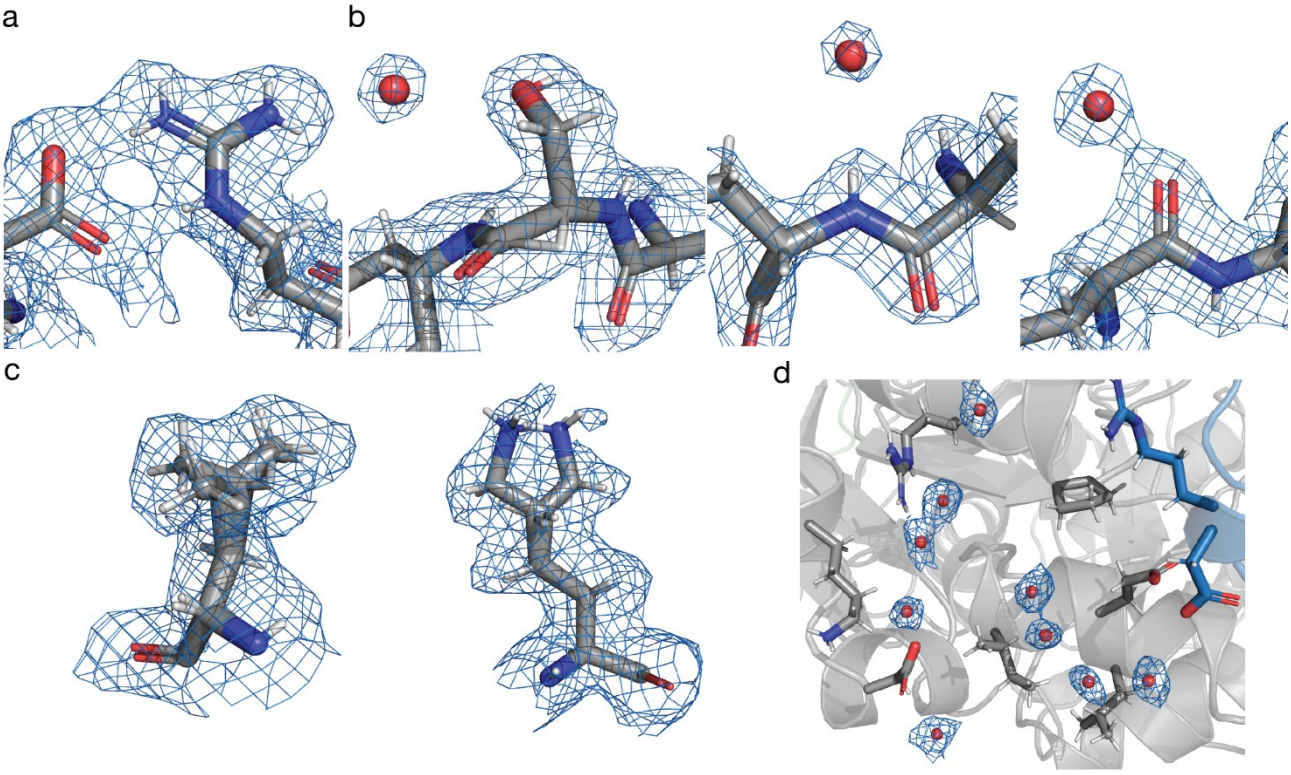

Supplementary Figure 8 High-resolution structural features can be readily seen in the cryo-EM map. **a)** Salt bridge between D69 and R63. **b)** Side chain hydration of S17 and back bone hydration of the oxygen and the nitrogen, respectively. **c)** alternative side chain conformations of L406 and K2. d) network of waters between two ureC proteins (grey, blue).

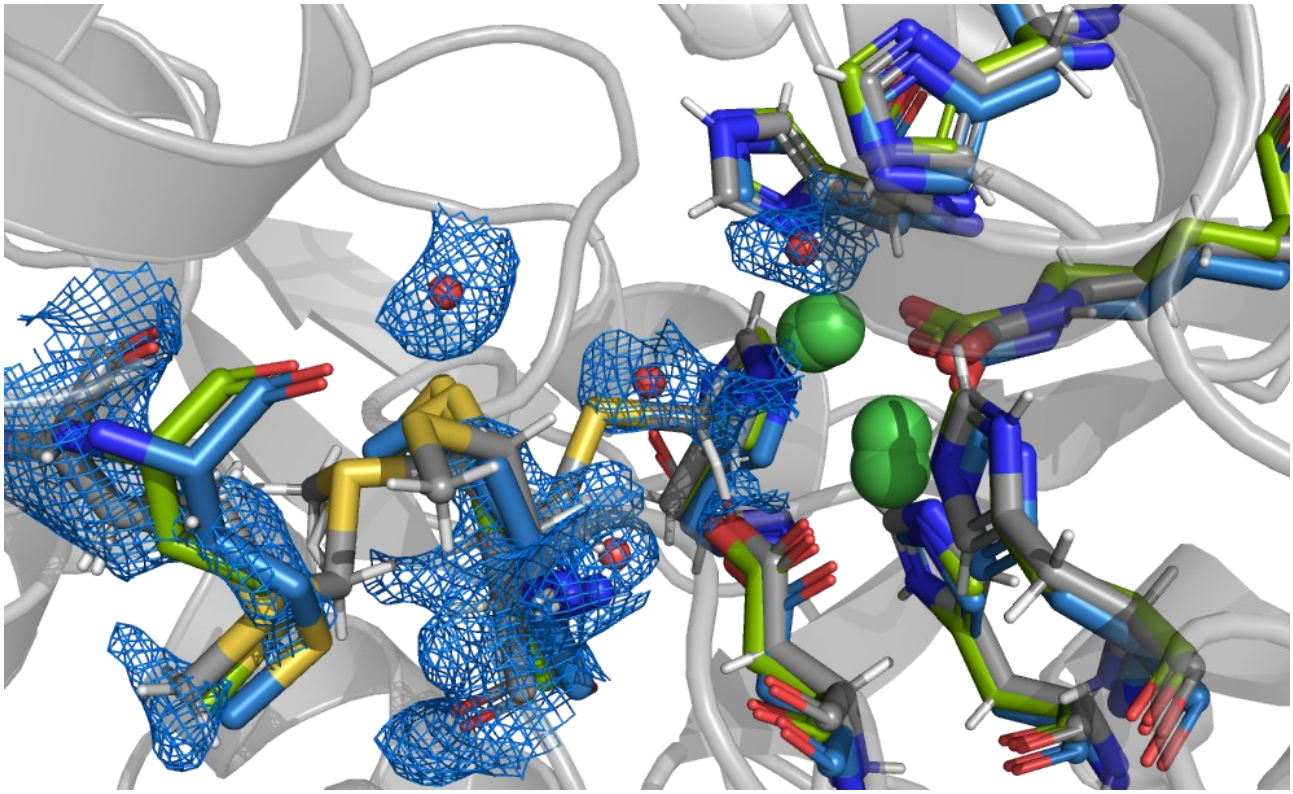

715

716 **Supplementary Figure 9** MET369 can adopt different conformations in the absence of the
717 substrate or an inhibitor. *Y. enterocolitica* urease (grey), *S. pasteurii* urease (blue), *K.*
718 *aerogenes* urease (green). One conformation could potentially reach the active site. There
719 is no described function for this amino acid in the catalysis. The conformation close to the
720 active site is only possible because the pocket is empty, which can be seen with an overlay
721 of the active site from *K. aerogenes* urease (PDB: 1EJW) at 1.9 Å and *S. pasteurii* urease
722 (PDB: 5OL4) at 1.28 Å resolution, respectively **(Figure 5d,e).**

723 # Supplementary Movies

724 **Supplementary Movie 1** Overview and feature highlights of the *Yersinia enterocolitica*
725 urease cryo-EM structure.

726 **Supplementary Movie 2** Morphing between maps and models obtained from different sets
727 of frames along the exposure.

728 # Supplementary Tables

729 **Supplementary Table 1** Cryo-EM data collection and image processing summary.

	Single shot	Multi shot
Data collection		
Microscope	Titan Krios	Titan Krios
Voltage [kV]	300	300
Direct electron detector	Gatan K2	Gatan K2
Zero-loss energy filter	GIF (20 eV slit width)	GIF (20 eV slit width)
Physical pixel size [Å]	0.639	0.639
Super-resolution mode	No	No
Total exposure [e^-/Å²]	42	42
Exposure time [s]	8	8
Number of frames [per movie]	40	40
Movies acquired	2,252	2,243
Beam-image shift?	No	3 shots per hole
Image processing (before merging)		
Movies processed	2,115	2,197
Pixel size [Å]	0.639	0.639
Box size [pixels²]	512	512
Particles picked (Gautomatch w/ templates)	87,204	107,399
Particles after 2D classification	87,032	80,239
Particles after 3D classification	51,173	62,884
Unmasked resolution [Å] (FSC 0.143)	2.52	2.39
Masked resolution [Å] (FSC 0.143)	2.20	2.10
Image processing (after merging)		
Particles in final reconstruction		119,020
Unmasked resolution [Å] (FSC 0.143)		2.20
Masked resolution [Å] (FSC 0.143)		1.98
Angular distribution efficiency (0 to 1)		0.60

730

731 **Supplementary Table 2** Beam tilt estimation after merging the two datasets.

	Multi-shot #1	**Multi-shot #2**	**Multi-shot #3**	**Single-shot**
Beamtilt x *(mrad)*	0.008	-0.218	-0.028	-0.078
Beamtilt y *(mrad)*	-0.091	-0.127	-0.000	-0.065

732

733 **Supplementary Table 3** Bayesian polishing training results.

	Multi Shot ***(before merging)***	**Single Shot** ***(before merging)***	**Merged**	**Multi Shot #1**	**Multi Shot #2**	**Multi Shot #3**	**Single shot**
Number of particles in training ***(approximate)***	5,000	5,000	10,000	10,000	10,000	10,000	10,000
Sigma for Velocity (Å/dose) ***(smaller = shorter tracks)***	0.531	0.819	0.779	0.810	0.693	0.636	0.681
Sigma for Divergence (Å) ***(higher = more homogeneous tracks across micrograph, i.e. "rigid block")***	3,600	10,455	10,620	10,260	7,350	5,220	8,355
Sigma for Acceleration (Å/dose) ***(smaller = straighter tracks)***	2.175	3.735	1.620	1.485	1.425	1.500	0.795

734

735 **Supplementary Table 4** Sequence identity between different ureases and *Y. enterocolitica*
736 urease.

Organism	PDB code	Nr. Of Genes	Stoichiometry α-(β)-(γ)	ureA (%)	ureB (%)	ureC (%)
S. pasteurii	5O4L	3	3-3-3	60.6	46.7	57.5
K. aerogenes	1EJW	3	3-3-3	60.6	52.9	58.7
H. pylori	1E9Z	2	12-12	52.0	50.4	57.6

737

738 **Supplementary Table 5** RMSD values between each chain of our *Y. enterocolitica* urease
739 model versus structures deposited at the PDB. Values are given in Ångstroms. Values in
740 parenthesis indicate the number of Cα atom pairs matched with and without pruning. The
741 program matchmaker from UCSF Chimera was used to calculate sequence alignments and
742 RMSD values between each chain in respective models.

	Chain A	Chain B	Chain C	Active site
1E9Z	0.860/0.942 (98/100)	0.702/4.424 (107/124)	0.642/1.248 (537/561)	0.634
Alignment Score	339.8	376.8	1874.2	-
5OL4	0.706/0.706 (100/100)	0.756/2.999 (108/120)	0.673/1.171 (542/563)	0.293
Alignment Score	369.3	327.5	2002.7	-
1EJW	0.607/0.607 (100/100)	0.622/1.054 (97/101)	0.611/0.916 (538/559)	0.270
Alignment Score	637.2	269.4	1957.0	-

743

Supplementary Note 1

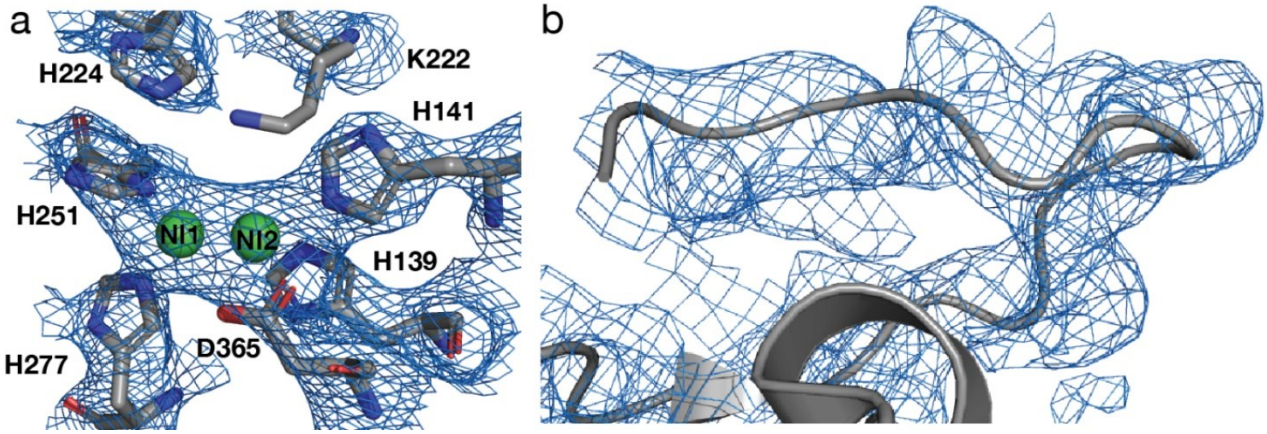

Supplementary Figure 10 Low resolution crystal structure of *Y. enterocolitica* urease. Structure determination by X-ray crystallography yielded a 3.01 Å resolution density, which was sufficient to see the higher oligomeric state of *Y. enterocolitica* urease, but not for detailed analysis of the assembly mechanism and active site.

Comparison of the model based on the high-resolution cryo-EM data *vs.* the previous crystal structure shows a few differences. The previous X-ray model did not include residue 100 of ureA and residues 31-33, 148-162 of ureB. Residues 148-162 form a helix, which was previously not observable. This helix sits right at the interface between three ureB proteins and constitutes the interaction between the trimers.

755 # Supplementary Methods

756 For X-ray crystallographic analysis of the *Y. enterocolitica* urease, *Y. enterocolitica* was
757 differently purified than described in the **Methods** for cryo-EM. The protein was precipitated
758 using 40-60% w/v ammonium sulfate, resuspended and dialyzed in 0.15M NaCl, 50mM Tris
759 pH 8.0. It was further purified using a 45 ml self-packed DEAE FF XK26/20 (Sigma, DFF100)
760 and a Superdex 200 10/300 GL column. The SEC was also used for buffer exchange to 20
761 mM HEPES, 100 mM NaCl pH 7. Urease crystals grew at 20°C at 10 mg/ml in 0.1M CHES
762 pH 9.5; 50% (v/v) PEG 200. Urease crystals belonged to space group H32 with unit cell
763 parameters of a= 157.2 Å, b = 157.2 Å and c= 774.6 Å, with four molecules per asymmetric
764 unit. The structure was determined by molecular replacement with PHASER (McCoy *et al.*,
765 2007) using the urease crystal structure from *Klebsiella aerogenes* (PDB: 1FWB) (Pearson
766 *et al.*, 1997). Model building and structure refinement were performed with Coot (Emsley &
767 Cowtan, 2004) and Buster-TNT (Blanc *et al.*, 2004). The atomic coordinates for this model
768 have been deposited in the Protein Data Bank under the accession code 4Z42.

769 # Supplementary References

770 Adams, P. D., Grosse-Kunstleve, R. W., Hung, L.-W., Ioerger, T. R., McCoy, A. J., Moriarty, N. W.,
771 Read, R. J., Sacchettini, J. C., Sauter, N. K. & Terwilliger, T. C. (2002). *Acta Crystallogr. Sect.*
772 *D*. **58**, 1948–1954.

773 Afonine, P. V, Klaholz, B. P., Moriarty, N. W., Poon, B. K., Sobolev, O. V, Terwilliger, T. C., Adams,
774 P. D. & Urzhumtsev, A. (2018). *Acta Crystallogr. Sect. D Struct. Biol.* **74**, 814–840.

775 Afonine, P. V, Poon, B. K., Read, R. J., Sobolev, O. V, Terwilliger, T. C., Urzhumtsev, A. & Adams,
776 P. D. (2018). *Acta Crystallogr. Sect. D*. **74**, 531–544.

777 Arnold, S. A., Albiez, S., Bieri, A., Syntychaki, A., Adaixo, R., Mcleod, R. A., Goldie, K. N.,
778 Stahlberg, H. & Braun, T. (2016). *J. Struct. Biol.* **197**, 0–6.

779 Ashkenazy, H., Abadi, S., Martz, E., Chay, O., Mayrose, I., Pupko, T. & Ben-Tal, N. (2016). *Nucleic*
780 *Acids Res.* **44**, W344–W350.

781 Benini, S., Rypniewski, W. R., Wilson, K. S., Ciurli, S. & Mangani, S. (1998). *JBIC J. Biol. Inorg.*
782 *Chem.* **3**, 268–273.

783 Berezin, C., Glaser, F., Rosenberg, J., Paz, I., Pupko, T., Fariselli, P., Casadio, R. & Ben-Tal, N.
784 (2004). *Bioinformatics*. **20**, 1322–1324.

785 Biyani, N., Righetto, R. D., McLeod, R., Caujolle-Bert, D., Castano-Diez, D., Goldie, K. N. &
786 Stahlberg, H. (2017). *J. Struct. Biol.* **198**, 124–133.

787 Blanc, E., Roversi, P., Vonrhein, C., Flensburg, C., Lea, S. M. & Bricogne, G. (2004). *Acta*
788 *Crystallogr. Sect. D Biol. Crystallogr.* **60**, 2210–2221.

789 Brilot, A. F., Chen, J. Z., Cheng, A., Pan, J., Harrison, S. C., Potter, C. S., Carragher, B.,
790 Henderson, R. & Grigorieff, N. (2012). *J. Struct. Biol.* **177**, 630–637.

791 Cardone, G., Heymann, J. B. & Steven, A. C. (2013). *J. Struct. Biol.* **184**, 226–236.

792 Chen, S., McMullan, G., Faruqi, A. R., Murshudov, G. N., Short, J. M., Scheres, S. H. W. &
793 Henderson, R. (2013). *Ultramicroscopy*. **135**, 24–35.

794 Cheng, A., Eng, E. T., Alink, L., Rice, W. J., Jordan, K. D., Kim, L. Y., Potter, C. S. & Carragher, B.
795 (2018). *J. Struct. Biol.* **204**, 270–275.

796 Cock, P. J. A., Antao, T., Chang, J. T., Chapman, B. A., Cox, C. J., Dalke, A., Friedberg, I.,
797 Hamelryck, T., Kauff, F., Wilczynski, B. & de Hoon, M. J. L. (2009). *Bioinformatics*. **25**, 1422–
798 1423.

799 Dixon, N. E., Gazzola, C., Blakeley, R. L. & Zerner, B. (1975). *J. Am. Chem. Soc.* **97**, 4131–4133.

800 Drummond, N., Murphy, B. P., Ringwood, T., Prentice, M. B., Buckley, J. F. & Fanning, S. (2012).
801 *Foodborne Pathog. Dis.* **9**, 179–189.

802 Emsley, P. & Cowtan, K. (2004). *Acta Crystallogr. Sect. D*. **60**, 2126–2132.

803 Fromm, S. A., Bharat, T. A. M., Jakobi, A. J., Hagen, W. J. H. & Sachse, C. (2015). *J. Struct. Biol.*
804 **189**, 87–97.

805 Goddard, T. D., Huang, C. C., Meng, E. C., Pettersen, E. F., Couch, G. S., Morris, J. H. & Ferrin,
806 T. E. (2018). *Protein Sci.* **27**, 14–25.

807 Grant, T. & Grigorieff, N. (2015). *Elife*. **4**,.

808 Gripenberg-Lerche, C., Zhang, L., Ahtonen, P., Toivanen, P. & Skurnik, M. (2000). *Infect. Immun.*
809 **68**, 942–947.

810 Ha, N.-C., Oh, S.-T., Sung, J. Y., Cha, K. A., Lee, M. H. & Oh, B.-H. (2001). *Nat. Struct. Biol.* **8**,
811 505.

812 Harauz, G. & van Heel, M. (1986). *Optik (Stuttg).* **78**, 146–156.

813 Hattne, J., Shi, D., Glynn, C., Zee, C., Gallagher-Jones, M., Martynowycz, M. W., Rodriguez, J. A.
814 & Gonen, T. (2018). *Structure*. **26**, 759-766.e4.

815 Jabri, E., Carr, M., Hausinger, R. & Karplus, P. (1995). *Science (80-.).* **268**, 998–1004.

816 Kappaun, K., Regina, A., Regina, C. & Ligabue-braun, R. (2018). *J. Adv. Res.* **13**, 3–17.

817 Kearse, M., Moir, R., Wilson, A., Stones-Havas, S., Cheung, M., Sturrock, S., Buxton, S., Cooper,
818 A., Markowitz, S., Duran, C., Thierer, T., Ashton, B., Meintjes, P. & Drummond, A. (2012).
819 *Bioinformatics*. **28**, 1647–1649.

820 Krissinel, E. & Henrick, K. (2007). *J. Mol. Biol.* **372**, 774–797.

821 Ligabue-Braun, R., Andreis, F. C., Verli, H. & Carlini, C. R. (2013). *Naturwissenschaften*. **100**,
822 459–467.

823 Madeira, F., Park, Y. M., Lee, J., Buso, N., Gur, T., Madhusoodanan, N., Basutkar, P., Tivey, A. R.
824 N., Potter, S. C., Finn, R. D. & Lopez, R. (2019). *Nucleic Acids Res.* **47**, W636–W641.

825 Maroney, M. J. & Ciurli, S. (2014). *Chem. Rev.* **114**, 4206–4228.

826 Mazzei, L., Cianci, M., Contaldo, U., Musiani, F. & Ciurli, S. (2017). *Biochemistry*. **56**, 5391–5404.

827 McCoy, A. J., Grosse-Kunstleve, R. W., Adams, P. D., Winn, M. D., Storoni, L. C. & Read, R. J.
828 (2007). *J. Appl. Crystallogr.* **40**, 658–674.

829 Naydenova, K. & Russo, C. J. (2017). *Nat. Commun.* **8**, 629.

830 Pearson, M. A., Michel, L. O., Hausinger, R. P. & Karplus, P. A. (1997). *Biochemistry*. **36**, 8164–
831 8172.

832 Pettersen, E. F., Goddard, T. D., Huang, C. C., Couch, G. S., Greenblatt, D. M., Meng, E. C. &
833 Ferrin, T. E. (2004). *J. Comput. Chem.* **25**, 1605–1612.

834 Podschun, R. & Ullmann, U. (1998). *Clin. Microbiol. Rev.* **11**, 589–603.

835 Punjani, A., Rubinstein, J. L., Fleet, D. J. & Brubaker, M. A. (2017). *Nat. Methods*. **14**, 290–296.

836 Rohou, A. & Grigorieff, N. (2015). *J. Struct. Biol.* **192**, 216–221.

837 Rokita, E., Makristathis, A., Hirschl, A. M. & Rotter, M. L. (2000). *J. Chromatogr. B Biomed. Sci.*
838 *Appl.* **737**, 203–212.

839 Rosenthal, P. B. & Henderson, R. (2003). *J. Mol. Biol.* **333**, 721–745.

840 Scheres, S. H. W. W. & Chen, S. (2012). *Nat. Methods*. **9**, 853–854.

841 Schorb, M., Haberbosch, I., Hagen, W. J. H., Schwab, Y. & Mastronarde, D. N. (2019). *Nat.*
842 *Methods*.

843 Sumner, J. B. (1926). *J. Biol. Chem.* **69**, 435–441.

844 Weatherburn, M. W. (1967). *Anal. Chem.* **39**, 971–974.

845 Yano, J., Kern, J., Irrgang, K.-D., Latimer, M. J., Bergmann, U., Glatzel, P., Pushkar, Y., Biesiadka,
846 J., Loll, B., Sauer, K., Messinger, J., Zouni, A. & Yachandra, V. K. (2005). *Proc. Natl. Acad.*
847 *Sci.* **102**, 12047–12052.

848 Young, G. M., Amid, D. & Miller, V. L. (1996). *J. Bacteriol.* **178**, 6487–6495.

849 Zheng, S. Q., Palovcak, E., Armache, J.-P., Verba, K. A., Cheng, Y. & Agard, D. A. (2017). *Nat.*
850 *Methods*. **14**, 331–332.

851 Zivanov, J., Nakane, T., Forsberg, B. O., Kimanius, D., Hagen, W. J., Lindahl, E. & Scheres, S. H.
852 (2018). *Elife*. **7**, e42166.

853 Zivanov, J., Nakane, T. & Scheres, S. H. W. (2019*a*). *IUCrJ*. **6**,.

854 Zivanov, J., Nakane, T. & Scheres, S. H. W. (2019*b*). *BioRxiv*. 798066.

855